2017

Microwave Bessel-Beam Propagation through Spatially Inhomogeneous Media

Ryan Francis Grecco
University of Vermont

Microwave Bessel-Beam Propagation through Spatially Inhomogeneous Media

A Thesis Presented

by

Ryan F. Grecco

to

The Faculty of the Graduate College

of

The University of Vermont

In Partial Fullfillment of the Requirements
for the Degree of Master of Science
Specializing in Electrical Engineering

May, 2017

Defense Date: September 21, 2016
Thesis Examination Committee:

Kurt E. Oughstun, Ph.D., Advisor
Darren L. Hitt, Ph.D., Chairperson
Tian Xia, Ph.D.
Cynthia J. Forehand, Ph.D., Dean of Graduate College

Abstract

Long range wireless power transmission (WPT) is a critical technology for the development of remote power systems for air and space vehicles as well as for point-to-point transmission on Earth. This can be achieved using either a laser for transmission in the infrared to optical frequency domain or by using microwaves. The objective of this research is to study the application of microwave power transmission (MPT) through the use of a so-called Bessel-beam whose unique propagation properties include a self-healing ability as well as non-diffractive properties. These two unique properties lead to an increase in the efficiency of microwave power transmission. In this research the propagation of a microwave Bessel-beam through a spatially inhomogeneous medium will be simulated in MATLAB using a plane wave spectrum representation of the electromagnetic beam field. The spatially inhomogeneous medium of interest here is the Earth's atmosphere whose electromagnetic properties (dielectric permittivity and electric conductivity) vary with altitude up through the ionosphere. The purpose of this research is to determine how efficiently a microwave Bessel beam can propagate in point-to-point transmission through the Earth's atmosphere as well as between satellites in Earth orbit.

Dedication

To my parents who have supported me every step of the way, to my friends for their continuous motivation, and to Kenzie for all her love and patience.

Acknowledgements

The research presented here has been supported by the Vermont Space Grant Consortium.

The largest thanks of course to my advisor and mentor, Dr. Kurt E. Oughstun, who I have worked with throughout the past year.

Table of Contents

List of Figures

List of Tables

Chapter 1

Introduction

1.1 Motivation

The study of electromagnetic beam propagation through inhomogeneous media is of central importance to many applications of electromagnetic theory. A complete understanding of this phenomena may be determined through a study of how efficiently the power contained in an electromagnetic beam can be propagated through a series of dielectric slabs. This includes the analysis of spatially dependent electromagnetic phenomena and the reflection and transmission of an electromagnetic field at an interface across which the dielectric permittivity and electric conductivity change.

The foremost reason for conducting this research is its application to wireless power transmission (WPT) systems. Specifically, this research investigates the use of Bessel-beam microwave radiation to transmit electromagnetic power from one point to another without the use of any material conductors. Advancements in WPT technology may serve to advance and possibly eliminate the aging power grid.

In general, WPT refers to the transmission of electrical energy from a power source

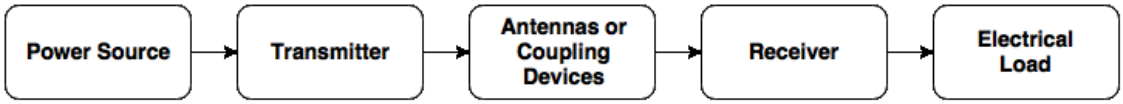

Figure 1.1: Generic block diagram of wireless power system.

to a load without the use of a material conductor. WPT depends on technologies that transmit and receive an electromagnetic field. A WPT system typically consists of a power source, a transmitter circuit, transmitting and receiving antennas, coupling devices, a receiver circuit, and an electrical load. A diagram representing a general WPT system is shown in Fig. 1.1. Functionally, the transmitter circuit converts electrical energy provided by the power source into a time-varying electromagnetic beam field and transmits the power contained in that field to a receiver antenna where the electrical power is converted and supplied to an electrical load.

The study of long range (over 1,000 meters) WPT systems has additional complications introduced by the presence of any spatial inhomogeneity in the region between the transmitter and receiver. This research is focused on the application of so-called Bessel-beams in order to overcome, at least in part, some of these complications. Bessel-beams possess both a nondiffractive property and an inherent self-healing ability [1] which may serve to overcome the aforementioned limiting effects introduced by spatial inhomogeneities.

1.2 Historical Overview

The basic idea of wireless power transmission was first conceived by Nikola Tesla in 1891. The technique used for the implementation of a WPT system is defined as being either non-radiative or radiative. Non-radiative WPT, being the most common

technique, transfers power using either a magnetic or an electric field. For example, a magnetic field can be manipulated to achieve magnetic inductive coupling between a pair of conducting coils. In a similar manner, wireless power may also be transferred by an electric field using capacitive coupling between metallic electrodes.

Beginning in 1891, Tesla investigated WPT using a radio frequency resonant transformer called a Tesla coil. This patented electrical device produced high-voltage (5 to 30 kV) and high-frequency (50 kHz to 10 MHz) alternating currents. This allowed Tesla to transmit electrical energy wirelessly over short distances (several meters) by means of resonant magnetic inductive coupling. Throughout this time period Tesla demonstrated this technology during a series of lectures where he would wirelessly power several lamps in the demonstration hall [2].

Tesla believed that WPT technology was the future of electrical power distribution and dedicated the majority of his remaining life to the development of a large scale WPT system. He moved his laboratory to Colorado Springs in 1899 where he developed a larger version of the Tesla coil. This device was capable of powering three incandescent lamps from over 100 feet away through resonant inductive coupling. Next, he set out to develop a system that could assist in transmitting power globally. In 1901, Tesla began constructing the Wardenclyffe Tower, a high-voltage WPT system located in Shoreham, New York. However, this project was never completed as his primary financial backer (J. P. Morgan) withdrew funding when Tesla informed him of the greater purpose of the project, to wirelessly transmit power long distances. Tesla spent the remaining years of his life defending his futuristic idea for a global WPT system.

The technological demands of World War II brought about the practical possi-

bility of radiative (far-field) techniques. Radiative techniques refer to power being transferred by directed beams of electromagnetic radiation. The frequency of the electromagnetic radiation used in this type of application is either in the microwave domain or in the optical domain of the spectrum using a laser beam. This technique is primarily used in systems where the transmitter and receiver are separated by a large distance.

1.2.1 Non-Radiative Power Transmission

Non-radiative power transmission is the most common technique used in commercial WPT systems today. The technique is most effectively used for relatively small range applications, including electric toothbrush and cell phone charging. The most common technique used in commercial applications is inductive coupling. Other techniques related to non-radiative power transfer include capacitive coupling, electrical conduction and magnetodynamic coupling.

Inductive coupling refers to power being transferred between coils of wire by a magnetic field. A block diagram of an inductive wireless power system is presented in Fig 1.2. A power source supplies electrical energy to an oscillator circuit which converts it to a high frequency alternating current. The transmitter and receiver together then form a transformer. An alternating current flowing through the transmitting coil creates an oscillating magnetic field, as described by Ampere's law, $\nabla \times \mathbf{H} = \mathbf{J} + \partial \mathbf{D}/\partial t$ [3]. This oscillating magnetic field then passes through the recieving coil where it induces an alternating electromotive force as described by Faraday's law of induction, $\nabla \times \mathbf{E} = -\partial \mathbf{B}/\partial t$ [3], which then creates an alternating current in the receiver. The induced alternating current can then be used to either supply

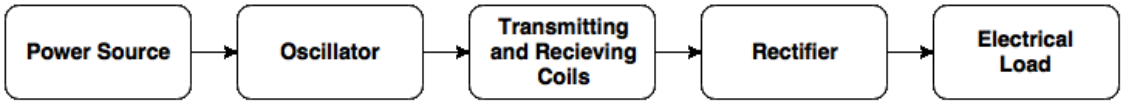

Figure 1.2: Generic block diagram of an inductive coupling wireless power system.

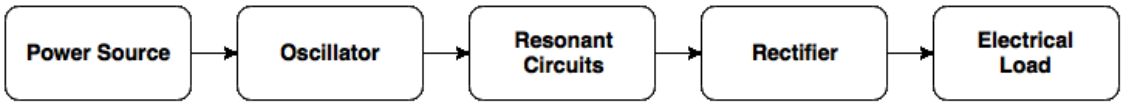

Figure 1.3: Generic block diagram of a resonant inductive coupling wireless power system.

power to the load directly or it can be rectified into direct current by a rectifier in the receiver.

A more efficient form of inductive coupling is known as resonant inductive coupling, as illustrated in Fig 1.3. In this technique power is transferred once again by a magnetic field, but in this case the power transfer is between two resonant circuits that are tuned to a resonance frequency that is common to the transmitter and receiver.

1.2.2 Radiative Power Transmission

Far-field radiative power transmission techniques are not widely used in power transmission systems. Though they have been tested experimentally, they have yet to be used in consumer applications. Radiative power transmission techniques have not yet been proven to be as efficient as standard power transmission techniques using wires.

Microwave power transmission allows for longer distance power transmission with shorter wavelengths of electromagnetic radiation. A microwave power transmission (MPT) system consists of an input power source, a microwave emitter, and a microwave receiver, as depicted in Fig. 1.4. A basic microwave receiver consists of an

array of rectifying antennas (a combination of an antenna and a rectifying circuit), referred to as a rectenna.

The first feasibility study of a MPT system was conducted by William C. Brown at Raytheon in 1965 [4]. The purpose of this experiment was to power an airborne microwave supported platform. The platform consisted of a miniature helicopter equipped with a rectenna array. In this experiment the miniature helicopter was continuously powered by a microwave beam for ten hours at an altitude of 50 feet, with an average transmission efficiency that was greater than 90% [4].

A later experiment of note was conducted by the NASA Jet Propulsion Laboratory in 1975 [5]. This experiment was a "step-up" from Brown's experiment in regards to the amount of power being transferred. Specifically, 30 kW of DC output power was transmitted wirelessly a distance of 1.54 km [5]. The ratio of the total DC power output to the integrated total available RF power incident on the receiver array was greater than 80% [5].

1.2.3 Objective of the Project

The primary objective of this research is to investigate a method of propagating a microwave beam through a spatially inhomogeneous medium more efficiently than current technologies allow. The method referred to here is the propagation of microwave power with a so-called Bessel-beam. The unique properties of a Bessel beam could allow for higher efficiency in MPT. With greater efficiency in MPT, current aerospace systems and electrical grid infrastructure could be revamped to accommodate a global WPT system.

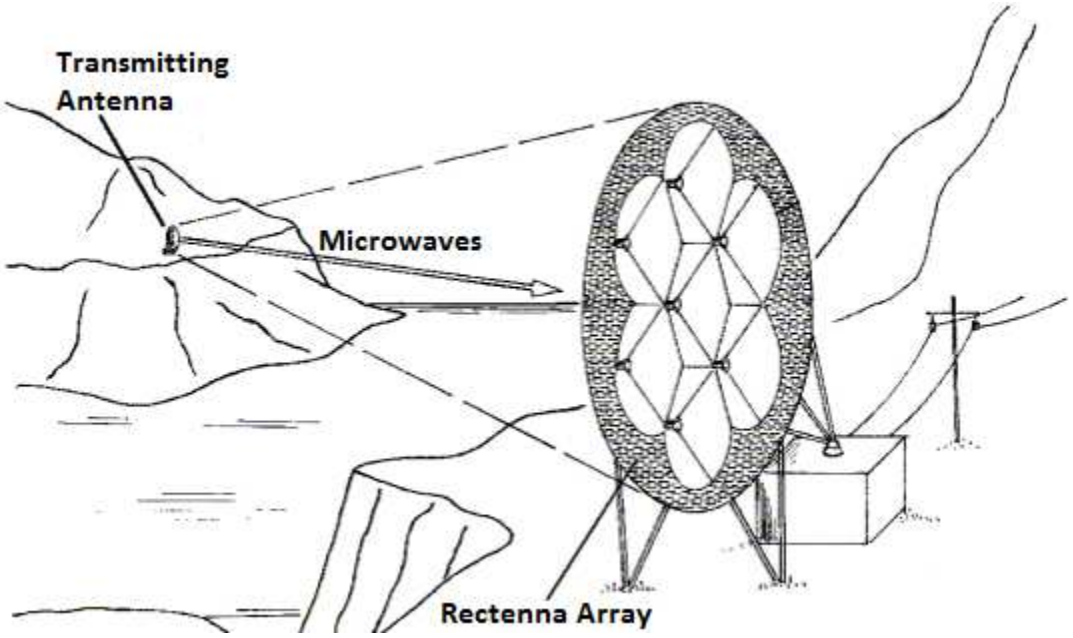

Figure 1.4: Microwave power transmission system [5].

1.3 Thesis Overview

This thesis begins with a discussion of the necessary fundamental background from electromagnetic theory. It includes a brief overview of Maxwell's equations leading into the development of electromagnetic wave modes. This pair of orthogonal wave modes are considered to be either transverse electric or transverse magnetic with respect to the direction of propagation. Following this development, the description of a spatially inhomogeneous medium is considered. The inhomogeneous medium investigated in this thesis is the Earth's atmosphere. The electromagnetic properties considered include the electric conductivity $\sigma(\omega)$, the dielectric permittivity $\epsilon(\omega)$, the magnetic permeability $\mu(\omega)$, the refractive index $n(\omega)$, and the impedance $Z(\omega)$. An electromagnetic Bessel-beam is then introduced and applied, through a numerical

simulation, to microwave beam propagation through the Earth's atmosphere. The numerical results presented include an assessment of how well a microwave Bessel-beam propagates through Earth's atmosphere and point-to-point in free space.

Chapter 2

Fundamental Theory and Mathematical Preliminaries

2.1 Macroscopic Maxwell's Equations

The macroscopic Maxwell equations describe the interdependence of the electric field $\mathscr{E}(\mathbf{r},t)$ and the magnetic field $\mathscr{B}(\mathbf{r},t)$ vectors through a set of coupled equations given, in differential form, by [6]

$$\nabla \cdot \mathscr{D}(\mathbf{r},t) = \rho(\mathbf{r},t), \tag{2.1a}$$

$$\nabla \cdot \mathscr{B} = 0, \tag{2.1b}$$

$$\nabla \times \mathscr{E} = -\frac{\partial}{\partial t}\mathscr{B}(\mathbf{r},t), \tag{2.1c}$$

$$\nabla \times \mathscr{H} = \frac{\partial}{\partial t}\mathscr{D}(\mathbf{r},t) + \mathscr{J}(\mathbf{r},t). \tag{2.1d}$$

in MKS units, where $\mathscr{D}(\mathbf{r},t)$ is the displacement vector (in *coloumb/m*^{2}), $\rho(\mathbf{r},t)$ is the charge density (in *coloumb/m*^{3}), $\mathscr{E}(\mathbf{r},t)$ is the electric field intensity vector (in *volt/m*), $\mathscr{B}(\mathbf{r},t)$ is the magnetic induction vector (in *tesla*), $\mathscr{H}(\mathbf{r},t)$ is the magnetic field intensity vector (in *ampere/m*), and $\mathscr{J}(\mathbf{r},t)$ is the current density vector (in *ampere/m*^{2}). The two divergence relations are know as Gauss's law for the electric and magnetic fields, respectively. The first curl relation is derived from Faraday's law and the second from Ampére's law [3]. This self-consistent set of equations was first formulated by Maxwell [3] through the inclusion of the displacement current $\partial\mathscr{D}(\mathbf{r},t)/\partial t$ in Ampére's law.

The charge and current densities appearing in Maxwell's equations are not independent quantities. From the physical law of conservation of charge, the charge density $\rho(\mathbf{r},t)$ and current density $\mathscr{J}(\mathbf{r},t)$, which describes the flow of charge, are related by the *equation of continuity*

$$\nabla\cdot\mathscr{J}(\mathbf{r},t)+\frac{\partial}{\partial t}\rho(\mathbf{r},t)=0. \tag{2.2}$$

This equation of continuity is contained in Maxwell's equations, as can be seen by the substitution of Eq. (2.1a) into the divergence of Eq. (2.1d). Finally, this set of field equations is connected to physical measurement through the Lorentz force relation

$$\mathscr{F}(\mathbf{r},t)=q\left(\mathscr{E}(\mathbf{r},t)+\mathbf{v}(\mathbf{r},t)\times\mathscr{B}(\mathbf{r},t)\right), \tag{2.3}$$

where $\mathscr{F}(\mathbf{r},t)$ is the force acting on a point charge q moving with velocity $\mathbf{v}(\mathbf{r},t)$ in vacuum.

2.2 Transverse Electric and Transverse Magnetic Modes

Consider the propagation of a time-harmonic electromagnetic field in an unbounded homogeneous, isotropic, conducting region of space. Maxwell's equations in source-free regions of space are given by [6]

$$\nabla \cdot \boldsymbol{\mathscr{E}} = 0, \tag{2.4a}$$

$$\nabla \cdot \boldsymbol{\mathscr{H}} = 0, \tag{2.4b}$$

$$\nabla \times \boldsymbol{\mathscr{E}} = -\frac{\partial \boldsymbol{\mathscr{B}}}{\partial t}, \tag{2.4c}$$

$$\nabla \times \boldsymbol{\mathscr{H}} = \frac{\partial \boldsymbol{\mathscr{D}}}{\partial t} + \boldsymbol{\mathscr{J}}, \tag{2.4d}$$

in MKS units, where

$$\boldsymbol{\mathscr{B}}(\mathbf{r}, t) = \int_{-\infty}^{t} \hat{\mu}(t - t') \boldsymbol{\mathscr{H}}(\mathbf{r}, t') dt' \tag{2.5}$$

is the magnetic induction field vector,

$$\boldsymbol{\mathscr{D}}(\mathbf{r}, t) = \int_{-\infty}^{t} \hat{\epsilon}(t - t') \boldsymbol{\mathscr{E}}(\mathbf{r}, t') dt' \tag{2.6}$$

is the electric displacement vector, and

$$\boldsymbol{\mathscr{J}}_c(\mathbf{r}, t) = \int_{-\infty}^{t} \hat{\sigma}(t - t') \boldsymbol{\mathscr{E}}(\mathbf{r}, t') dt' \tag{2.7}$$

is the conduction current density. For a strictly monochromatic field of angular frequency ω, one sets

$$\boldsymbol{\mathscr{E}}(\mathbf{r},t) = \Re\left\{\mathbf{E}(\mathbf{r})e^{i\omega t}\right\}, \tag{2.8a}$$

$$\boldsymbol{\mathscr{H}}(\mathbf{r},t) = \Re\left\{\mathbf{H}(\mathbf{r})e^{i\omega t}\right\}, \tag{2.8b}$$

where $\mathbf{E}$ and $\mathbf{H}$ are the complex phasor representations of the electric and magnetic field vectors. With this substitution, Maxwell's equations (2.4) assume their time-harmonic (or phasor) form

$$\nabla \cdot \mathbf{E} = 0, \tag{2.9a}$$

$$\nabla \cdot \mathbf{H} = 0, \tag{2.9b}$$

$$\nabla \times \mathbf{E} = -i\omega\mu(\omega)\mathbf{H}, \tag{2.9c}$$

$$\nabla \times \mathbf{H} = i\omega\epsilon_c(\omega)\mathbf{E}, \tag{2.9d}$$

after application of the convolution theorem, where

$$\mu(\omega) = \int_{-\infty}^{\infty} \hat{\mu}(t)e^{i\omega t}dt, \tag{2.10a}$$

$$\epsilon(\omega) = \int_{-\infty}^{\infty} \hat{\epsilon}(t)e^{i\omega t}dt, \tag{2.10b}$$

$$\sigma(\omega) = \int_{-\infty}^{\infty} \hat{\sigma}(t)e^{i\omega t}dt, \tag{2.10c}$$

are the magnetic permeability, dielectric permittivity and electric conductivity, respectfully. The complex permittivity appearing in Eq. (2.9d) is defined as

$$\epsilon_c(\omega) = \epsilon(\omega) + i\frac{\sigma(\omega)}{\omega} \tag{2.11}$$

and will be touched upon again in Chapter 3. Upon taking the curl of Eq. (2.9c) and using Eqs. (2.9a) and (2.9d), one obtains

$$\underbrace{\nabla \times (\nabla \times \mathbf{E})}_{\nabla \underbrace{(\nabla \cdot \mathbf{E})}_{0} - \nabla^2 \mathbf{E}} = -i\mu\omega \underbrace{\nabla \times \mathbf{H}}_{i\epsilon_c \omega \mathbf{E}}$$

$$\therefore \quad \nabla^2 \mathbf{E} + \mu\epsilon_c\omega^2 \mathbf{E} = \mathbf{0}. \tag{2.12}$$

Similarly, upon taking the curl of Eq. (2.9d) and using (2.9b) and (2.9c), there results

$$\underbrace{\nabla \times (\nabla \times \mathbf{H})}_{\nabla \underbrace{(\nabla \cdot \mathbf{H})}_{0} - \nabla^2 \mathbf{H}} = i\omega\epsilon_c \underbrace{\nabla \times \mathbf{E}}_{i\mu\omega \mathbf{H}}$$

$$\therefore \quad \nabla^2 \mathbf{H} + \mu\epsilon\omega^2 \mathbf{H} = \mathbf{0}. \tag{2.13}$$

The wavenumber of the monochromatic field is given by

$$\begin{aligned} \tilde{k}(\omega) &= \omega \left[\mu\epsilon(\omega)\right]^{1/2} \\ &= \frac{\omega}{c} n(\omega) \end{aligned} \tag{2.14}$$

where $n(\omega)$ is the refractive index of the medium defined as

$$n(\omega) = \left[\frac{\mu\epsilon(\omega)}{\mu_0\epsilon_0}\right]^{1/2}, \tag{2.15}$$

where $c = 1/\sqrt{\mu_0\epsilon_0}$ is the speed of light in a vacuum. With these identifications, Eqs. (2.13) and (2.14) become

$$\nabla^2\mathbf{E} + \tilde{k}^2(\omega)\mathbf{E} = \mathbf{0} \tag{2.16}$$

$$\nabla^2\mathbf{H} + \tilde{k}^2(\omega)\mathbf{H} = \mathbf{0}. \tag{2.17}$$

These equations are known as the Helmholtz equations [3].

2.2.1 TE and TM Modes in Rectangular Coordinates

The phasor electric and magnetic field vectors in rectangular coordinates for a time-harmonic electromagnetic wave propagating in the z-direction may then be represented in component form as

$$\mathbf{E} = \hat{1}_x E_x + \hat{1}_y E_y + \hat{1}_z E_z, \tag{2.18a}$$

$$\mathbf{H} = \hat{1}_x H_x + \hat{1}_y H_y + \hat{1}_z H_z. \tag{2.18b}$$

With this substitution the field equations (2.9) become

$$\frac{\partial E_x}{\partial x} + \cancel{\frac{\partial E_y}{\partial y}} + \frac{\partial E_z}{\partial z} = 0 \tag{2.19a}$$

$$\frac{\partial H_x}{\partial x} + \cancel{\frac{\partial H_y}{\partial y}} + \frac{\partial H_z}{\partial z} = 0 \tag{2.19b}$$

$$\cancel{\frac{\partial E_z}{\partial y}} - \frac{\partial E_y}{\partial z} = -i\mu\omega H_x \tag{2.19c}$$

$$\frac{\partial E_x}{\partial z} - \frac{\partial E_z}{\partial x} = -i\mu\omega H_y \tag{2.19d}$$

$$\frac{\partial E_y}{\partial x} - \cancel{\frac{\partial E_x}{\partial y}} = -i\mu\omega H_z \tag{2.19e}$$

$$\cancel{\frac{\partial H_z}{\partial y}} - \frac{\partial H_y}{\partial z} = i\epsilon\omega E_x \tag{2.19f}$$

$$\frac{\partial H_x}{\partial z} - \frac{\partial H_z}{\partial x} = i\epsilon\omega E_y \tag{2.19g}$$

$$\frac{\partial H_y}{\partial x} - \cancel{\frac{\partial H_x}{\partial y}} = i\epsilon\omega E_z \tag{2.19h}$$

In order to simplify the analysis, attention is now turned to "two dimensional" dielectric regions in which there is no spatial variation of the field vectors along the y-direction, so that $\partial/\partial y = 0$ for each component of each field vector. The above set of equations then separates into two distinct groups as follows:

$$\left.\begin{aligned} \frac{\partial H_x}{\partial x} + \frac{\partial H_z}{\partial z} &= 0 \\ \frac{\partial E_y}{\partial z} &= i\mu\omega H_x \\ \frac{\partial E_y}{\partial x} &= -i\mu\omega H_z \\ \frac{\partial H_x}{\partial z} - \frac{\partial H_z}{\partial x} &= i\epsilon\omega E_y \end{aligned}\right\} \begin{aligned} \mathbf{E} &= \hat{1}_y E_y \\ \mathbf{H} &= \hat{1}_x H_x + \hat{1}_z H_z \end{aligned} \tag{2.20}$$

and

$$\left.\begin{aligned} \frac{\partial E_x}{\partial x} + \frac{\partial E_z}{\partial z} &= 0 \\ \frac{\partial E_x}{\partial z} - \frac{\partial E_z}{\partial x} &= -i\mu\omega H_y \\ \frac{\partial H_y}{\partial z} &= -i\epsilon\omega E_x \\ \frac{\partial H_y}{\partial x} &= i\epsilon\omega E_z \end{aligned}\right\} \begin{aligned} \mathbf{E} &= \hat{1}_x E_x + \hat{1}_z E_z \\ \mathbf{H} &= \hat{1}_y H_y \end{aligned} \tag{2.21}$$

Upon differentiating the second relation in Eq. (2.20) with respect to z and the third with respect to x and adding the two results yields, after use of the the first and fourth relations in Eq. (2.20),

$$\boxed{\begin{aligned} \frac{\partial^2 E_y}{\partial x^2} + \frac{\partial^2 E_y}{\partial z^2} + \frac{\omega^2}{c^2} n^2 E_y &= 0 \\ H_x = -\frac{i}{\mu\omega}\frac{\partial E_y}{\partial z} \\ H_z = \frac{i}{\mu\omega}\frac{\partial E_y}{\partial x} \end{aligned}} \quad \text{TE Modes} \tag{2.22}$$

where

$$\begin{aligned} \mathbf{E}_{\mathrm{TE}} &= \hat{1}_y E_y, \\ \mathbf{H}_{\mathrm{TE}} &= \hat{1}_x H_x + \hat{1}_z H_z. \end{aligned} \tag{2.23}$$

These are called TE modes because the electric field vector does not have a component along the propagation direction (the z-direction).

In a similar manner, differentiation of the third relation in Eq. (2.21) with respect to z and the fourth with respect to x and adding the two results together yields, after

use of the first and second relations in Eq. (2.21),

$$\boxed{\begin{array}{c}\dfrac{\partial^2 H_y}{\partial x^2}+\dfrac{\partial^2 H_y}{\partial z^2}+\dfrac{\omega^2}{c^2}n^2 H_y=0\\ E_x=\dfrac{i}{\epsilon\omega}\dfrac{\partial H_y}{\partial z}\\ E_z=-\dfrac{i}{\epsilon\omega}\dfrac{\partial H_y}{\partial x}\end{array}} \quad \text{TM Modes} \tag{2.24}$$

where

$$\begin{aligned}\mathbf{E}_{\mathrm{TM}}&=\hat{1}_x E_x+\hat{1}_z E_z\\ \mathbf{H}_{\mathrm{TM}}&=\hat{1}_y H_y.\end{aligned} \tag{2.25}$$

These are called TM modes because the magnetic field vector does not have a z-component. Notice that $\mathbf{E}_{\mathrm{TE}}\cdot\mathbf{E}_{\mathrm{TM}}=\mathbf{H}_{\mathrm{TE}}\cdot\mathbf{H}_{\mathrm{TM}}=0$ so that they are mutually orthogonal fields.

2.2.2 TE and TM Modes in Cylindrical Coordinates

In cylindrical coordinates (ρ,ϕ,z) the field vectors are expressed in the form

$$\mathbf{E}=\hat{1}_\rho E_\rho+\hat{1}_\phi E_\phi+\hat{1}_z E_z \tag{2.26a}$$

$$\mathbf{H}=\hat{1}_\rho H_\rho+\hat{1}_\phi H_\phi+\hat{1}_z H_z \tag{2.26b}$$

where $\rho=\sqrt{x^2+y^2}$ is the radial distance perpendicular to and from the z-axis and $\phi=\tan^{-1}(y/x)$ is the azimuthal angle measured from the positive x-axis. With this

substitution the field equations (2.9) take on the component form

$$\frac{1}{\rho}\frac{\partial(\rho E_\rho)}{\partial\rho} + \cancel{\frac{1}{\rho}\frac{\partial E_\phi}{\partial\phi}} + \frac{\partial E_z}{\partial z} = 0 \tag{2.27a}$$

$$\frac{1}{\rho}\frac{\partial(\rho H_\rho)}{\partial\rho} + \cancel{\frac{1}{\rho}\frac{\partial H_\phi}{\partial\phi}} + \frac{\partial H_z}{\partial z} = 0 \tag{2.27b}$$

$$\cancel{\frac{1}{\rho}\frac{\partial E_z}{\partial\phi}} - \frac{\partial E_\phi}{\partial z} = -i\mu\omega H_\rho \tag{2.27c}$$

$$\frac{\partial E_\rho}{\partial z} - \frac{\partial E_z}{\partial\rho} = -i\mu\omega H_\phi \tag{2.27d}$$

$$\frac{1}{\rho}\frac{\partial(\rho E_\phi)}{\partial\rho} - \cancel{\frac{1}{\rho}\frac{\partial E_\rho}{\partial\phi}} = -i\mu\omega H_z \tag{2.27e}$$

$$\cancel{\frac{1}{\rho}\frac{\partial H_z}{\partial\phi}} - \frac{\partial H_\phi}{\partial z} = i\epsilon\omega E_\rho \tag{2.27f}$$

$$\frac{\partial H_\rho}{\partial z} - \frac{\partial H_z}{\partial\rho} = i\epsilon\omega E_\phi \tag{2.27g}$$

$$\frac{1}{\rho}\frac{\partial(\rho H_\phi)}{\partial\rho} - \cancel{\frac{1}{\rho}\frac{\partial H_\rho}{\partial\phi}} = i\epsilon\omega E_z \tag{2.27h}$$

In order to simplify the analysis, attention is now turned to "azimuthally symmetric" geometries in which there is no spatial variation of the field vectors in the ϕ-direction, so that $\partial/\partial\phi = 0$ for each component of each field vector. The above set of equations then separates into two distinct groups as follows:

$$\left.\begin{aligned} \frac{1}{\rho}\frac{\partial(\rho H_\rho)}{\partial\rho} + \frac{\partial H_z}{\partial z} &= 0 \\ \frac{\partial E_\phi}{\partial z} &= i\mu\omega H_\rho \\ \frac{1}{\rho}\frac{\partial(\rho E_\phi)}{\partial\rho} &= -i\mu\omega H_z \\ \frac{\partial H_\rho}{\partial z} - \frac{\partial H_z}{\partial\rho} &= i\epsilon\omega E_\phi \end{aligned}\right\} \begin{aligned} \mathbf{E} &= \hat{1}_\phi E_\phi \\ \mathbf{H} &= \hat{1}_\rho H_\rho + \hat{1}_z H_z \end{aligned} \tag{2.28}$$

$$\left.\begin{aligned} \frac{1}{\rho}\frac{\partial(\rho E_\rho)}{\partial\rho} + \frac{\partial E_z}{\partial z} &= 0 \\ -\frac{\partial H_\phi}{\partial z} &= i\epsilon\omega E_\rho \\ \frac{1}{\rho}\frac{\partial(\rho H_\phi)}{\partial\rho} &= -i\epsilon\omega E_z \\ \frac{\partial E_\rho}{\partial z} - \frac{\partial E_z}{\partial\rho} &= i\mu\omega E_\phi \end{aligned}\right\} \begin{aligned} \mathbf{E} &= \hat{1}_\rho E_\rho + \hat{1}_z E_z \\ \mathbf{H} &= \hat{1}_\phi H_\phi \end{aligned} \tag{2.29}$$

Differentiation of the second relation in Eq. (2.28) with respect to z and the third with respect to ρ and adding the two results yields, after use of the the first and fourth relations in Eq. (2.28),

$$\boxed{\begin{aligned} \frac{1}{\rho}\frac{\partial}{\partial\rho}\frac{\rho\,\partial E_\phi}{\partial\rho} + \frac{\partial^2 E_\phi}{\partial z^2} + \frac{\omega^2}{c^2}n^2 E_\phi &= 0 \\ H_\rho = -\frac{i}{\mu\omega}\frac{\partial E_\phi}{\partial z} & \\ H_z = \frac{i}{\mu\omega\rho}\frac{\partial(\rho E_\phi)}{\partial\rho} & \end{aligned}} \quad \text{TE Modes} \tag{2.30}$$

where

$$\begin{aligned} \mathbf{E}_{\mathrm{TE}} &= \hat{1}_\phi E_\phi \\ \mathbf{H}_{\mathrm{TE}} &= \hat{1}_\rho H_\rho + \hat{1}_z H_z. \end{aligned} \tag{2.31}$$

These are called TE modes because the electric field vector does not have a z-component.

In a similar manner, differentiation of the second relation in Eq. (2.29) with respect to z and the third with respect to ρ and adding the two results together yields, after

use of the first and fourth relations in Eq. (2.29),

$$\boxed{\begin{array}{c} \dfrac{1}{\rho}\dfrac{\partial}{\partial\rho}\dfrac{\rho\,\partial H_\phi}{\partial\rho} + \dfrac{\partial^2 H_\phi}{\partial z^2} + \dfrac{\omega^2}{c^2}n^2 H_\phi = 0 \\ E_\rho = \dfrac{i}{\epsilon\omega}\dfrac{\partial H_\phi}{\partial z} \\ E_z = -\dfrac{i}{\epsilon\omega\rho}\dfrac{\partial(\rho H_\phi)}{\partial\rho} \end{array}} \quad \text{TM Modes} \tag{2.32}$$

where

$$\begin{aligned} \mathbf{E}_{\mathrm{TM}} &= \hat{1}_\rho E_\rho + \hat{1}_z E_z \\ \mathbf{H}_{\mathrm{TM}} &= \hat{1}_\phi H_\phi \end{aligned} \tag{2.33}$$

These are called TM modes because the magnetic field vector does not have a component along the propagation direction (the z-direction). The cylindrical TE and TM modes fields are mutually orthogonal. Any cylindrically symmetric field propagating in the z-direction may be expressed as a linear combination of TE and TM modes.

2.3 Gaussian Beam

A Gaussian beam is the fundamental beam type used to describe the outcoupled field from a stable laser system. Because of its known propagation properties, it is used in this research as the baseline to which the propagation properties of a Bessel-beam are compared.

The Gaussian beam is a radially symmetric beam whose initial electric field at $z = 0$ is described by

$$E_s = E_0 \exp\left(-\frac{r^2}{w_0^2}\right) \tag{2.34}$$

where r is the radial distance from the optical axis of the beam, and where w_0 is the

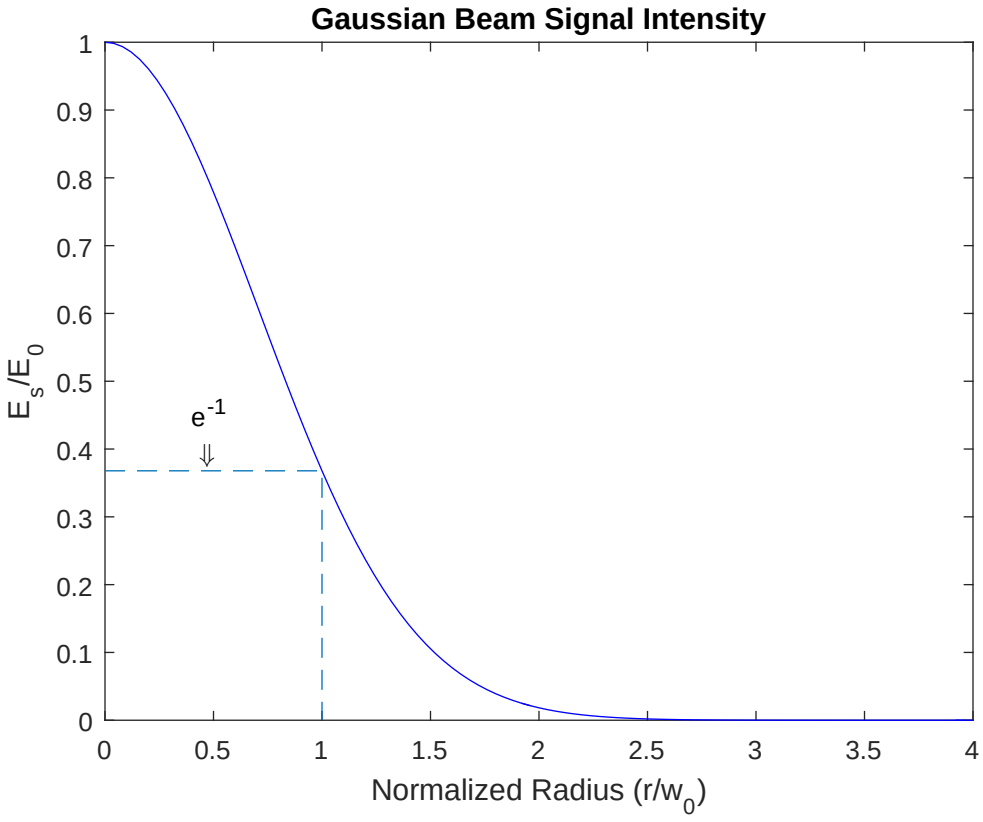

Figure 2.1: Gaussian electric field (E_s) as a function of the normalized radius.

Gaussian beam radius at which the point the initial field amplitude falls to e^{-1} of its on-axis value, as illustrated in Fig. 2.1.

The Gaussian beam width evolves according to the value $w(z)$ defining the radial beam width, where

$$w(z) = w_0\sqrt{1 + \left(\frac{z}{z_R}\right)^2}, \tag{2.35}$$

with

$$z_R = \frac{\pi w_0^2}{\lambda} \tag{2.36}$$

denoting the so-called Rayleigh range [6]. The Rayleigh range corresponds to the

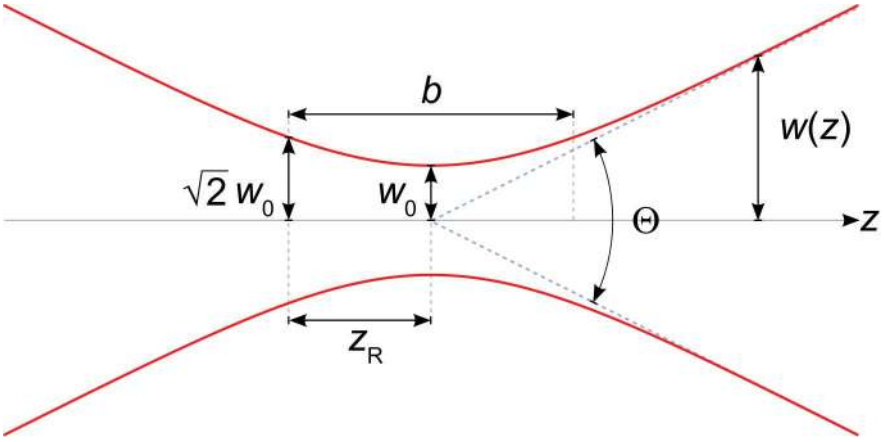

Figure 2.2: Gaussian beam width $\omega(z)$ as a function of the distance z along the beam.

distance z_R from the beam waist at $z = 0$ where the beam width $w(z)$ has increased to $\sqrt{2}$ times larger than its value $w(0) = w_0$ at $z = 0$. At this point the on-axis intensity has decreased to half of its peak value at $z = 0$.

As z becomes much greater than the Rayleigh range, the beam half-width $w(z)$ increases linearly with z. The angle describing the divergence of the beam is given by

$$\theta = \frac{\lambda}{\pi w_0}, \tag{2.37}$$

as illustrated in Fig. 2.2. The full angular spread of the beam far from the beam waist is then given by $\Theta = 2\theta$. Notice that the beam divergence is inversely proportional to the spot size for a given wavelength, so that a decrease in the beam waist size w_0 results in an increase of the beam divergence $\Theta = 2\theta$ accompanied by a decrease in the Rayleigh range z_R.

Chapter 3

Electromagnetic Characteristics of the Earth's Atmosphere

3.1 Spatially Inhomogeneous Media

Electromagnetic wave propagation is directly effected by the properties of the medium it is traveling through. The electromagnetic properties characterizing any given medium include the electric conductivity $\sigma(\omega)$ (in Siemens/meter or mhos/meter $\mho/m$), the dielectric permittivity $\epsilon(\omega)$ (in Farads/meter), and the magnetic permeability $\mu(\omega)$ (in Henries/meter). The refractive index $\mathrm{n}(\omega) = \sqrt{\epsilon(\omega)\mu(\omega)/\epsilon_0\mu_0}$, which is dimensionless, and impedance $\mathrm{Z}(\omega) = \sqrt{\mu(\omega)/\epsilon(\omega)}$ (in ohms (Ω)), are derived from these fundamental material parameters.

3.1.1 Earth's Atmosphere

With regards to its electromagnetic characteristics, the Earth's atmosphere is partitioned into three distinct vertical regions: a non-ionized region, an ionized region, and free-space. The non-ionized region extends from sea level up to approximately 90km above sea level. In this region, the electromagnetic characteristics are primarily affected by temperature, water vapor pressure and atmospheric pressure. The ionized region extends from 90km up to 1,000km above sea level. In this region the electromagnetic characteristics are primarily affected by the electron density, the electron and ion temperatures, and the ionic composition. The uppermost portion of the atmosphere is referred to as free-space, extending from 1,000km to 35,700km (geosynchronous orbit) above sea level. The properties in this region are defined to be those in a vacuum. The region above free-space is known as interplanetary space.

3.1.2 Mars' Atmosphere

The Martian atmosphere consists of a four regions, all of which are much less dense than the Earth's Atmosphere. The layers of Mars's atmosphere are known as the exosphere, thermosphere, middle atmosphere, and lower atmosphere [7]. The exosphere starts at about 200km above the surface of Mars and extends upwards to where the atmosphere merges with the vacuum of space. There is no distinct region where the atmosphere ends. The thermosphere is the region below the exosphere with very high temperatures caused by heating from the sun. In this region atmospheric gases start to separate from each other rather than forming the even mixture that exists at lower atmospheric layers. The middle atmosphere is the region in which Mars' jet

stream flows. The lower atmosphere is a relatively warm region affected by heat from airborne dust and the ground.

With regards to the electromagnetic properties of Mars's atmosphere, they can be deemed negligible. The Martian atmosphere is approximately 0.6% as dense as Earth's atmosphere [7]. Knowing this it can be assumed when running electromagnetic simulations of Mars's atmosphere that it can have the same properties as a vacuum.

3.2 Electric Conductivity

Electric conductivity $\sigma(\omega)$ is a measure of a materials ability to accommodate the transport of electric charge. This material parameter is measured in either Siemens per meter (S/m) or mhos per meter ($\mho$/m).

In the case of the Earth's atmosphere, the electric conductivity possesses three components, each dependent upon altitude. The parallel or field-aligned conductivity $\sigma_0(z)$ describes the conductivity in the direction parallel to the Earth's magnetic field. The field-aligned conductivity is by far the largest of the three Earth's conductivity components. The Pedersen conductivity $\sigma_1(z)$ is in the direction vertical to the Earth's magnetic field and parallel to the electric field originating at the magnetic poles. Finally, the Hall conductivity $\sigma_2(z)$ is in the direction vertical to both of these magnetic and electric fields. A comparison of the field-aligned conductivity $\sigma_0(z)$ and Pedersen conductivity $\sigma_1(z)$ as a function of altitude z above sea level is shown in Fig. 3.1. As can be seen, $\sigma_1(z)$ is at least 12 orders of magnitude down from $\sigma_0(z)$ throughout the Earth's atmosphere.

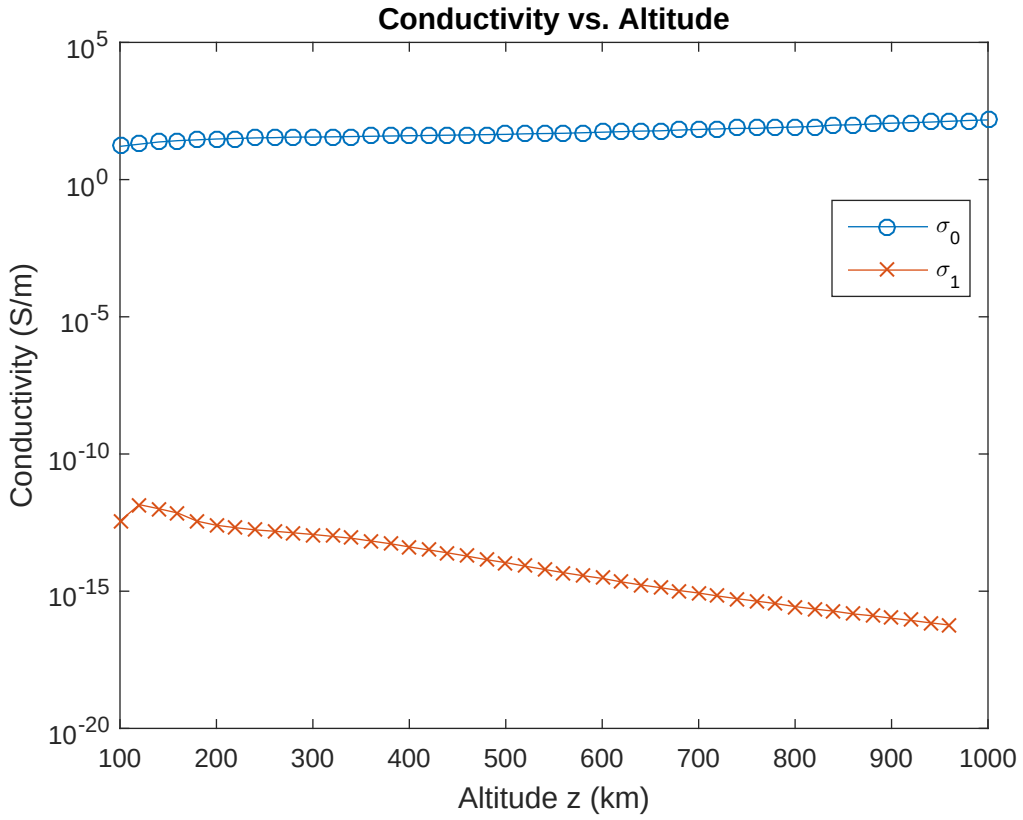

Figure 3.1: Field-aligned and Pedersen conductivity measured in S/m corresponding to specific altitudes in the first 1,000km of the Earth's atmosphere. Notice that the conductivity vanishes in the non-ionized region and in free space at altitudes higher than 1,000km. Data provided by Dao et al [8].

3.3 Dielectric Permittivity

The dielectric permittivity is a measure of the ability of a medium to capacitively store electric field energy and is accordingly measured in Farads per meter (F/m). The permittivity of free space is given by $\epsilon_0 = 8.845 \times 10^{-12}$ F/m. The permittivity $\epsilon(z, \omega)$ in a spatially inhomogeneous medium such as the Earth's atmosphere can be represented as

$$\epsilon(z, \omega) = \epsilon_0 \epsilon_r(z, \omega) \tag{3.1}$$

where $\epsilon_r(z, \omega) = \epsilon(z, \omega)/\epsilon_0$ is the relative permittivity of the medium [6]. The dependence of ϵ on the frequency of the electromagnetic field is known as temporal dispersion and its dependence on the distance z above sea-level is referred to as spatial inhomogeneity.

3.3.1 Complex Permittivity

The complex permittivity combines to dielectric permittivity $\epsilon(z, \omega)$ and electric conductivity into a single quantity that characterizes the frequency dependent electrical properties of the material. This was defined in Eq. (2.11) in connection with the phasor form of Ampére's law as

$$\epsilon_c(\omega) = \epsilon(\omega) + i\frac{\sigma(\omega)}{\omega}. \tag{3.2}$$

If the static conductivity $\sigma_0 = \sigma(0)$ is nonzero, then the complex permittivity has a simple pole at the origin $\omega = 0$. Furthermore this equation can be broken down into

real and imaginary parts as

$$\epsilon_c(\omega) = \left(\epsilon_r(\omega) - \frac{\sigma_i(\omega)}{\omega}\right) + i\left(\epsilon_i(\omega) + \frac{\sigma_r(\omega)}{\omega}\right), \tag{3.3}$$

where $\epsilon_r(\omega) = \Re\{\epsilon(\omega)\}$ is the real part of the permittivity, which is related to the reactively stored energy within the medium, and $\epsilon_i(\omega) = \Im\{\epsilon(\omega)\}$ is the imaginary part of the permittivity, which is related to the dissipation of energy within the medium [6]. Since the conductivity through the Earth's atmosphere is purely real the complex dielectric permittivity can be calculated, in this case, using

$$\epsilon_c(\omega) = \epsilon_r(\omega) + i\left(\epsilon_i(\omega) + \frac{\sigma_r(\omega)}{\omega}\right). \tag{3.4}$$

Using the previously shown values for the field-aligned conductivity and values for the permittivity from Dao et al. [8] the relative complex permittivity was calculated. The results are shown with respect to the altitude z in Fig. 3.2. It can be seen in Fig. 3.2 that because the conductivity is, within the approximation of the present analysis, purely real, the conductivity only has an effect on the imaginary part of the complex permittivity, as seen in Fig. 3.2 where the imaginary part and magnitude of the relative complex permittivity are overlapping.

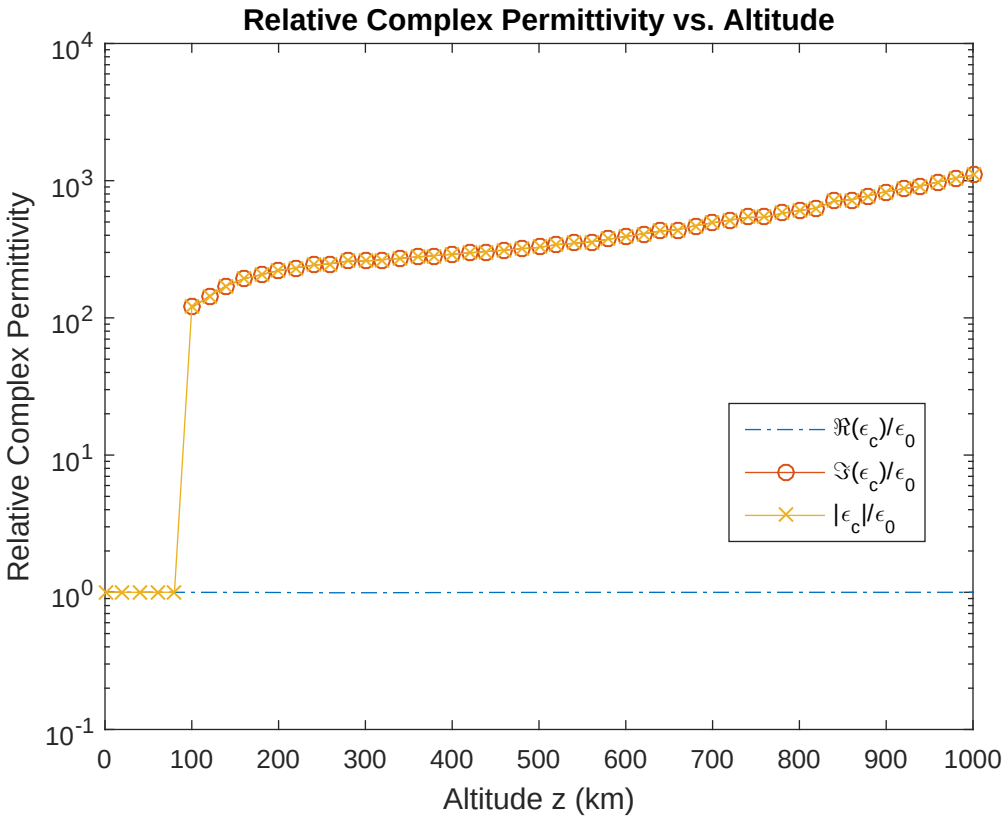

Figure 3.2: Complex permittivity (in F/m) corresponding to specific altitudes in the first 1,000km of the Earth's atmosphere. Notice that the magnitude and imaginary part of the relative complex permittivity are overlapping in the ionized region. Beyond the ionized region, the permittivity is that of free space. Data calculated using data published by Dao et al. [8].

3.4 Refractive Index

The refractive index is defined in terms of the complex dielectric permittivity and relative magnetic permeability as

$$\mathrm{n}(z,\omega) = \sqrt{\mu_r \frac{\epsilon_c(z,\omega)}{\epsilon_0}} \tag{3.5}$$

where μ_r is the relative magnetic permeability [6]. In the case of the Earth's atmosphere, $\mu_r \cong 1$. The calculated index of refraction corresponding to altitude is shown in Fig 3.3. Notice that the real and imaginary parts of the index of refraction are overlapping because the conductivity is purely real, having an equal effect on the real and imaginary parts.

3.5 Impedance

The impedance $\eta(z,\omega)$ of each layer of the atmosphere is related to its permittivity by the relation

$$\eta(z,\omega) = \sqrt{\frac{\mu_r}{\epsilon_c(\omega)/\epsilon_0}}\eta_0 \tag{3.6}$$

where $\eta_0 = \sqrt{\mu_0/\epsilon_0} = 377\Omega$ is the impedance of free space [9]. A plot of the complex intrinsic impedance of the Earth's atmosphere versus altitude z is illustrated in Fig. 3.4.

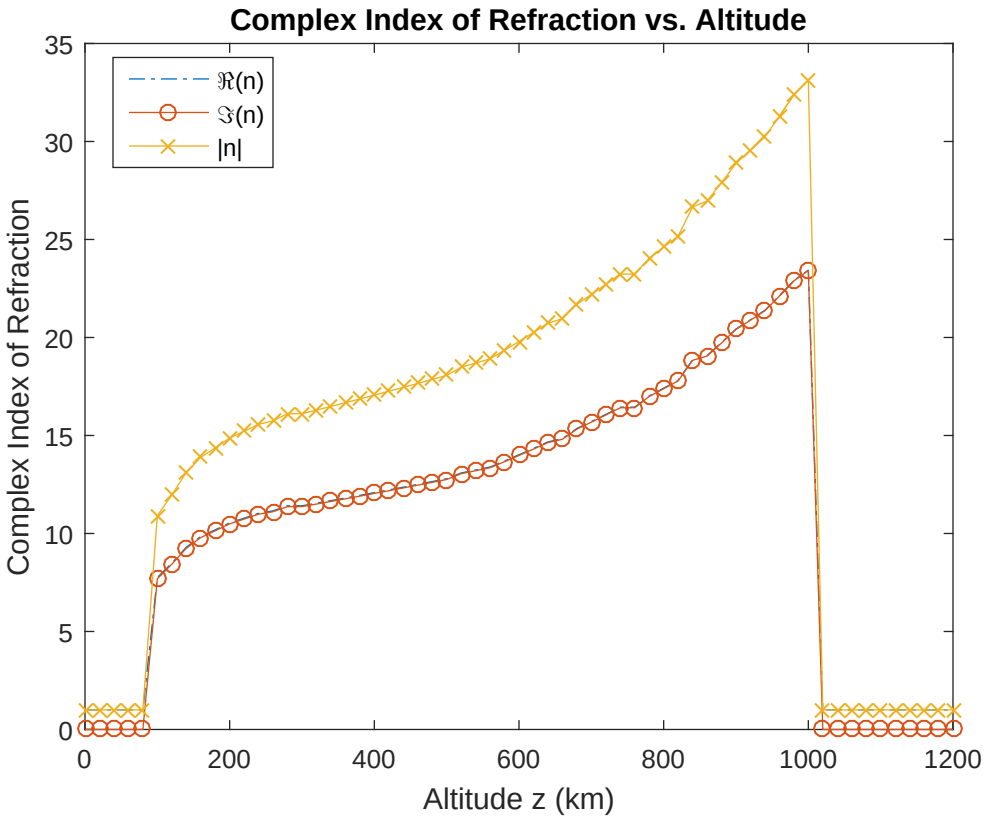

Figure 3.3: Complex index of refraction corresponding to specific altitudes in the first 1,000km of the Earth's atmosphere. The real and imaginary parts of the relative complex permittivity are overlapping in the ionized region. The magnitude and real parts of the refractive index beyond the ionized region and out into free space is one. Results based upon data published by Dao et al. [8].

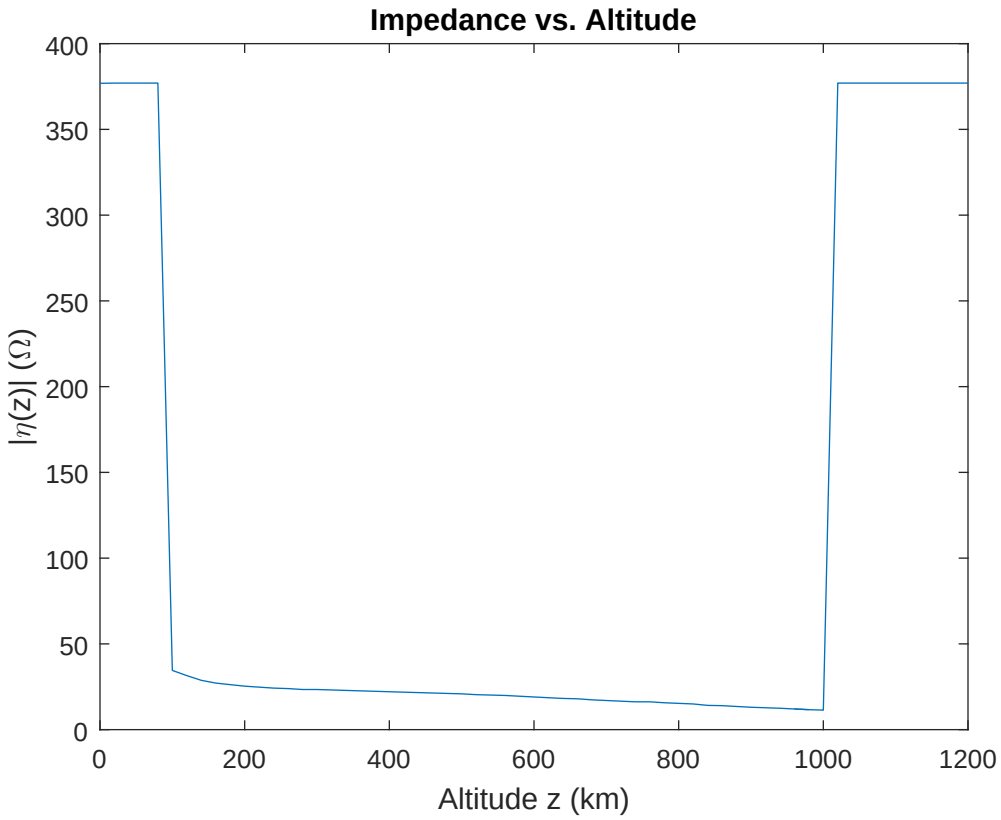

Figure 3.4: Magnitude of complex impedance corresponding to specific altitudes in the first 1,000km of Earth's atmosphere. The impedance increases back to $\eta_0 = 377\Omega$ for altitudes past the ionized region. Results based upon data published by Dao et al. [8].

3.6 Reflection and Transmission Coefficients

The reflection and transmission coefficients are determined by the impedance change from one layer to another. At each interface there is a corresponding reflection and transmission coefficient. The reflection coefficient Γ describes what fraction of the electric field amplitude is reflected back. The transmission coefficient τ describes what fraction of the electric field amplitude is transmitted in the forward direction. With regard to the layered atmosphere model considered here,

$$\Gamma_{ij} = \frac{\eta_j - \eta_i}{\eta_j + \eta_i} \tag{3.7}$$

and

$$\tau_{ij} = \frac{2\eta_j}{\eta_j + \eta_i} \tag{3.8}$$

where η_i is the impedance of the medium where the incident wave field resides and η_j is the impedance of the medium where the transmitted wave field resides [9]. A plot of the reflection and transmission coefficients is shown in Fig. 3.5 as a function of the interference number j. The vertical thickness of each layer is given by $\Delta z = 20$km so that the height of each layer above the Earth's surface is given by $z_j = j\Delta z$.

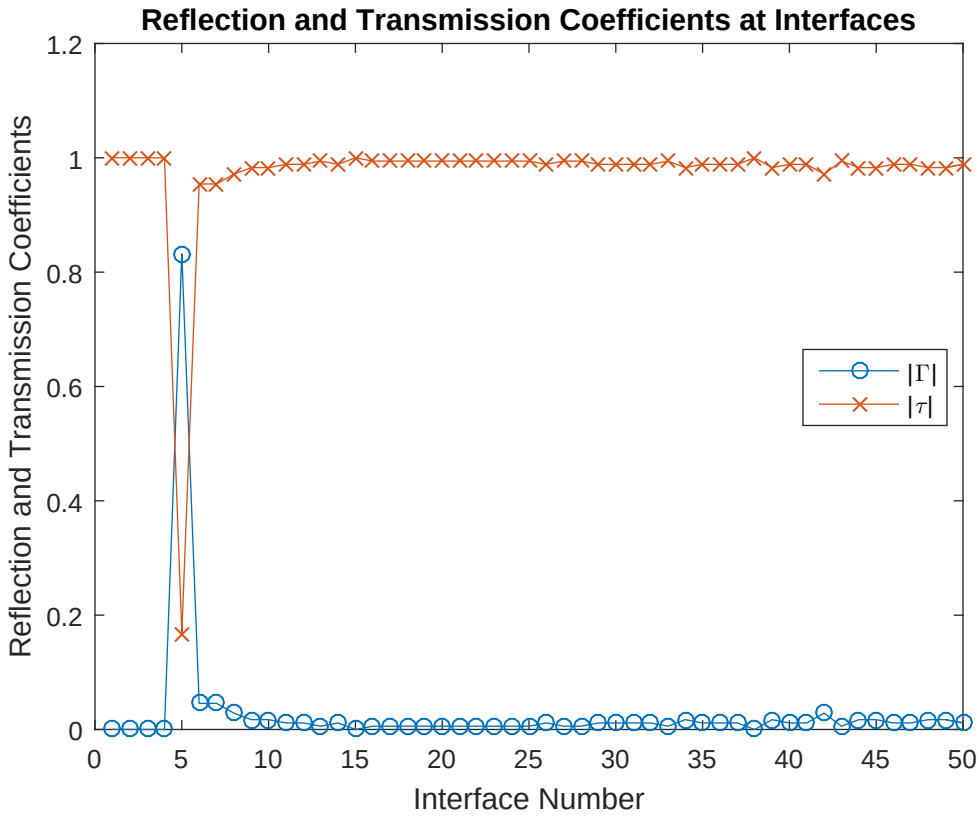

Figure 3.5: Reflection and Transmission coefficients corresponding to impedance interfaces in the first 1,000km of Earth's atmosphere. The large dip at interface 5 is due to a large impedance change from the non-ionized region to the ionized region of the Earth's atmosphere. At all other interfaces, practically all of the field is transmitted at each layer. Results based upon data published by Dao et al. [8].

Chapter 4

Electromagnetic Bessel Beam

4.1 Scalar Wave Formulation

The goal in this section is to deduce the form of a cylindrically symmetric plane wave that propagates in a vacuum, known as a Bessel beam. This is done based upon the derivation given by K. T. McDonald [10]. A scalar, azimuthally symmetric wave of frequency ω that propagates in the z-direction may be written as

$$\psi(\mathbf{r}, t) = f(\rho)e^{i(k_z z - \omega t)}, \tag{4.1}$$

where $\rho = \sqrt{x^2 + y^2}$. The problem is then to deduce the form of the radial function $f(\rho)$ together with any relevant condition on the wave number k_z, and then to relate Eq. (4.1) to a complete set of Maxwell's equations.

The first step is to determine the precise form of the radial function $f(\rho)$ that

satisfies the scalar wave equation

$$\nabla^2\psi = \frac{1}{c^2}\frac{\partial^2\psi}{\partial t^2}. \tag{4.2}$$

Substitution of Eq. (4.1) into this wave equation then yields

$$\frac{d^2f}{d\rho^2} + \frac{1}{\rho}\frac{df}{d\rho} + (k^2 - k_z^2) = 0. \tag{4.3}$$

This is precisely the differential equation defining Bessel functions of order 0, so that

$$f(\rho) = J_0(k_\rho\rho), \tag{4.4}$$

where

$$k_\rho^2 + k_z^2 = k^2. \tag{4.5}$$

The form of (4.5) suggests that we introduce a real parameter α such that

$$k_\rho = k\sin\alpha, \tag{4.6a}$$

$$k_z = k\cos\alpha. \tag{4.6b}$$

The desired cylindrical plane wave then assumes the form

$$\psi(\mathbf{r}, t) = J_0(k\rho\sin\alpha)e^{i(kz\cos\alpha - \omega t)}, \tag{4.7}$$

which is referred to as a Bessel beam [10].

4.2 Electromagnetic Formulation

The next step in the analysis is to determine each component of the electric and magnetic fields of a Bessel beam through Maxwell's equations. This is accomplished through the determination of the vector potential $\mathbf{A}$ from the scalar wave function $\psi(r,t)$ given in Eq. (4.7). This analysis is performed in the Lorenz gauge where the scalar potential Φ is related to the vector potential $\mathbf{A}$ through the Lorenz condition

$$\nabla \cdot \mathbf{A} + \epsilon_0 \mu_0 \frac{\partial \Phi}{\partial t} = 0. \tag{4.8}$$

The vector potential can therefore have a nonzero divergence. The electric and magnetic fields are then determined by the vector and scalar potentials as

$$\mathbf{E} = -\nabla\Phi - \frac{\partial \mathbf{A}}{\partial t}, \tag{4.9}$$

and

$$\mathbf{B} = \nabla \times \mathbf{A}. \tag{4.10}$$

The scalar potential is then determined from the vector potential using the Lorenz condition and the electric field then follows from Eq. (4.9). For a wave-field with constant frequency ω and time dependence of the form $e^{-i\omega t}$, so that $\partial\Phi/\partial t = -i\omega\Phi$. The Lorenz condition then yields

$$\tilde{\Phi} = -i\frac{c}{k}\nabla \cdot \tilde{\mathbf{A}}, \tag{4.11}$$

and the phasor electric field is then given by

$$\tilde{\mathbf{E}} = ick\left[\tilde{\mathbf{A}} + \frac{1}{k^2}\nabla(\nabla\cdot\tilde{\mathbf{A}})\right]. \tag{4.12}$$

Then, $\nabla\cdot\tilde{\mathbf{E}} = 0$ since $\nabla^2(\nabla\cdot\tilde{\mathbf{A}}) + k^2(\nabla\cdot\tilde{\mathbf{A}}) = 0$, which follows from the Helmholtz equation for the vector potential in the Lorenz gauge, given by $\nabla^2\tilde{\mathbf{A}} + k^2\tilde{\mathbf{A}} = 0$ for a vector potential $\tilde{\mathbf{A}}$ of frequency ω that satisfies Eq. (4.2). The scalar solution (4.7) to the wave equation is now taken as the z-component of the vector potential as

$$\tilde{A}_z(\mathbf{r},t) = \psi(\mathbf{r},t) \propto J_0(k\rho\sin\alpha)e^{i(kz\cos\alpha-\omega t)}, \tag{4.13}$$

so that the divergence of $\mathbf{A}$ is given by

$$\nabla\cdot\tilde{\mathbf{A}} = \frac{\partial\tilde{\psi}}{\partial z} = ik\cos\alpha J_0(k\rho\sin\alpha)e^{i(kz\cos\alpha-\omega t)}. \tag{4.14}$$

Substitution of this result into Eq. (4.12) with ∇ expressed in cylindrical coordinates then yields, after dividing the electric and magnetic fields by $k\sin\alpha$,

$$\tilde{E}_\rho = \cos\alpha J_1(k\rho\sin\alpha)e^{i(kz\cos\alpha-\omega t)}, \tag{4.15a}$$

$$\tilde{E}_\phi = 0, \tag{4.15b}$$

$$\tilde{E}_z = i\sin\alpha J_0(k\rho\sin\alpha)e^{i(kz\cos\alpha-\omega t)}, \tag{4.15c}$$

and

$$\tilde{B}_\rho = 0, \tag{4.16a}$$

$$\tilde{B}_\phi = J_1(k\rho \sin\alpha) e^{i(kz\cos\alpha - \omega t)}, \tag{4.16b}$$

$$\tilde{B}_z = 0. \tag{4.16c}$$

Because of the assumption made in Eq. (4.13), the Bessel-beam considered here is a transverse magnetic (TM) wave. The radial electric field E_ρ vanishes on the z axis, while the longitudinal electric field E_z is maximal there. Cylindrically symmetric waves with radial electric polarization are also known as axicon beams. As seen in Fig 4.1, the radial component of the electric field vanishes on the z-axis ($\rho = 0$) with an amplitude that slowly decreases from its maximum value just next to the z-axis. As seen in Fig. 4.2, the longitudinal component of the electric field E_z is purely imaginary. The amplitude of the imaginary component of the longitudinal electric field E_z slowly decreases to zero from its maximum value. As seen in Fig. 4.3, the amplitude of the angular component of the magnetic field B_ϕ slowly decreases from its maximum amplitude.

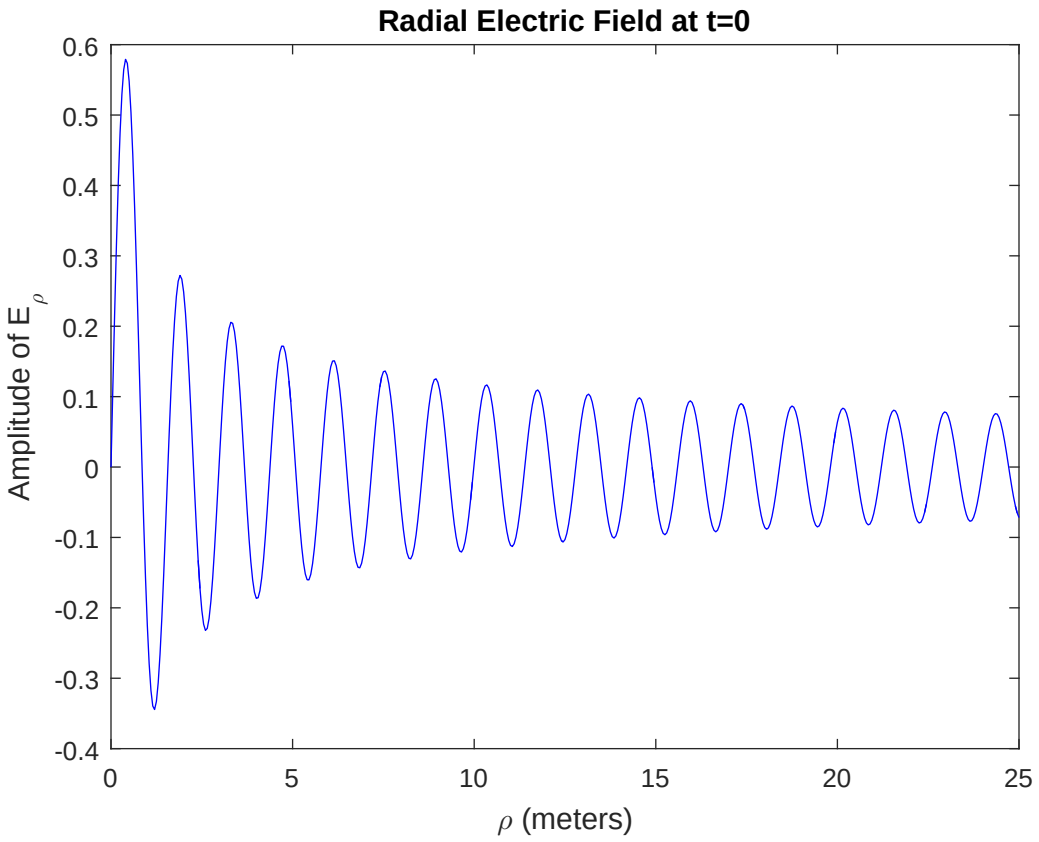

Figure 4.1: Radial electric field (E_ρ) as a function of the radial distance ρ from the z-axis.

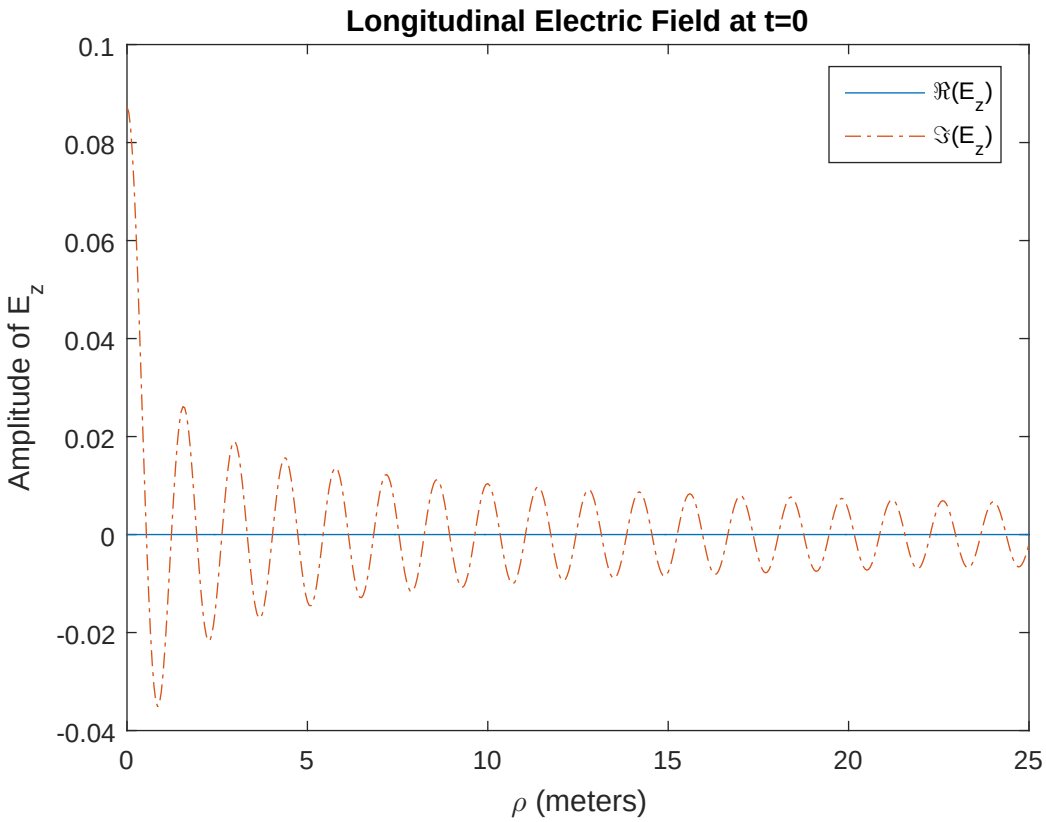

Figure 4.2: Longitudinal electric field (E_z) as a function of the radial distance ρ from the z-axis.

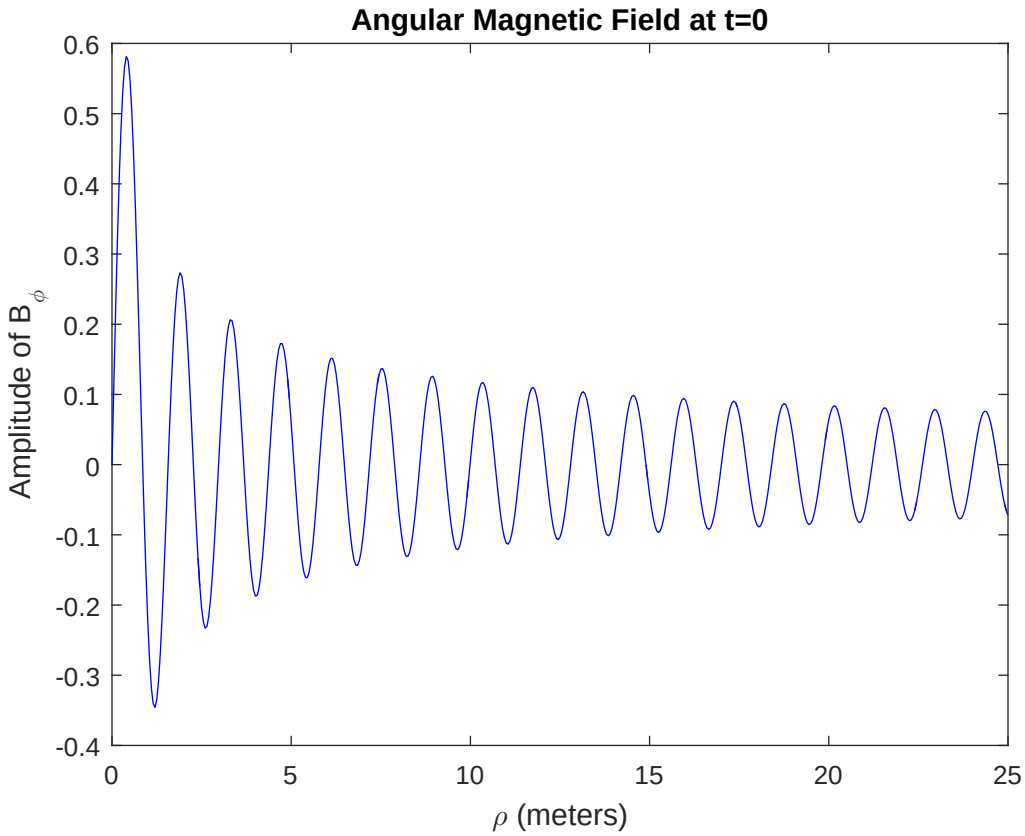

Figure 4.3: Angular magnetic field component (B_ϕ) as a function of the radial distance ρ from the z-axis.

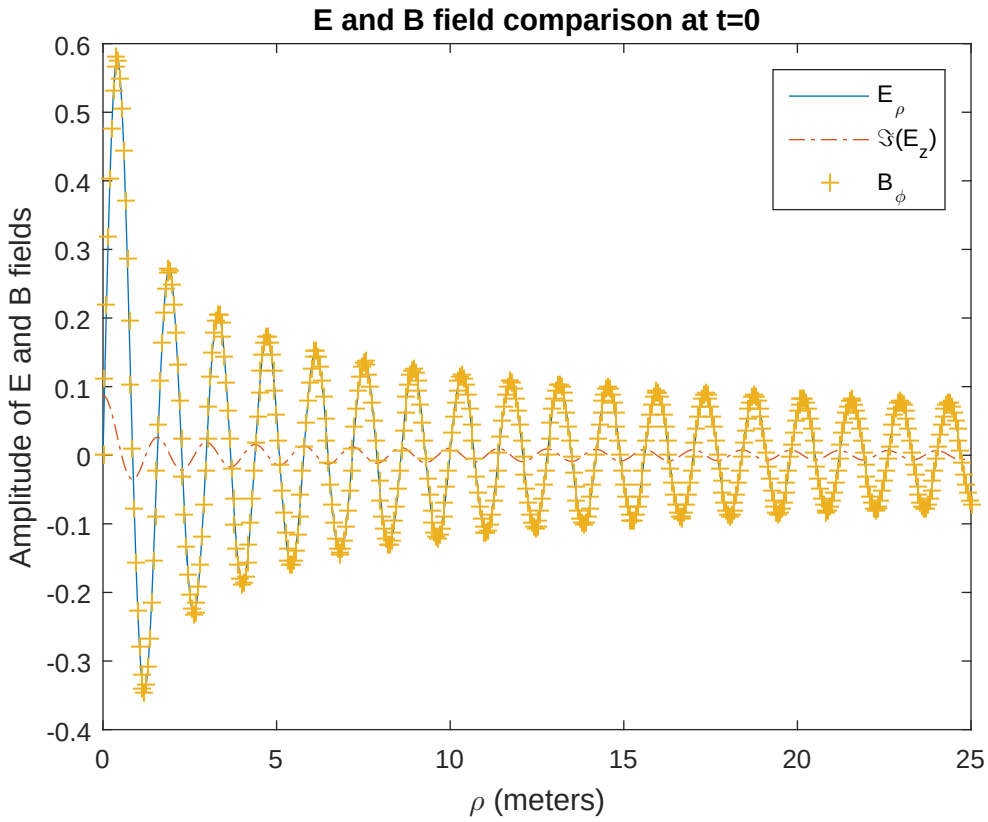

Figure 4.4: Comparison of the amplitudes of the radial electric field, imaginary part of the longitudinal electric field and the angular magnetic field as a function of the radius. The radial electric field and the angular magnetic field are overlapping.

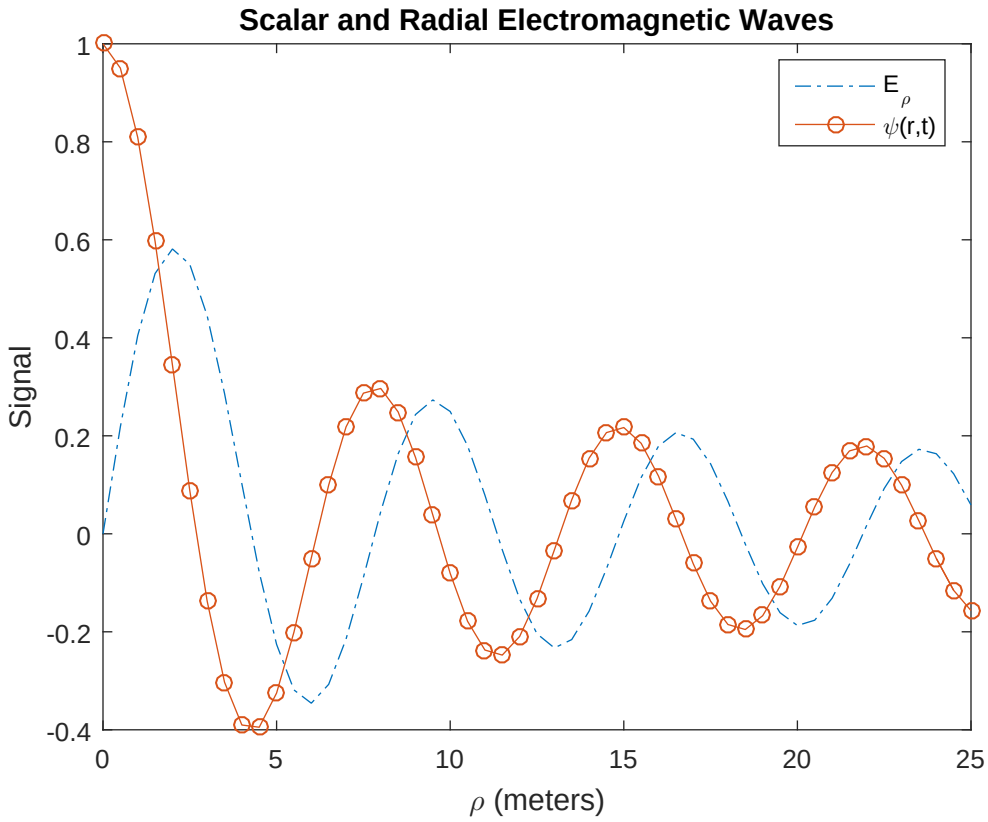

Figure 4.5: Comparison of the scalar wave equation and the radial electromagnetic fields.

4.3 Bessel-Beam Construction

The physical realization of a Bessel-beam has been achieved using a variety of experimental methods. Some of these methods produce what is considered a pseudo-Bessel-beam [1] and others a true Bessel-beam [1]. In the present research only the true mathematical model of a Bessel beam was considered and simulated.

The first Bessel-beam launcher reported in open literature consists of a diffracting ring placed at the focal distance of a convergent lens and illuminated by a plane wave [1], as shown in Fig. 4.6. Light diffracts as it passes through the ring. After passing through the lens, the diffracted rays interfere with each other and thereby form form a pseudo-Bessel-beam. This launcher suffers from very low efficiency because most of the beam power is blocked by the diaphragm. This problem can be overcome using an axicon lens, shown in Fig. 4.7, which is more commonly used today. An axicon lens has a flat entrance surface and an output volume shaped into a cone. When a plane wave is incident upon the conic surface, the light refracts into a converging conic beam and thereby forms a pseudo-Bessel-beam over the region of overlap illustrated in the figure.

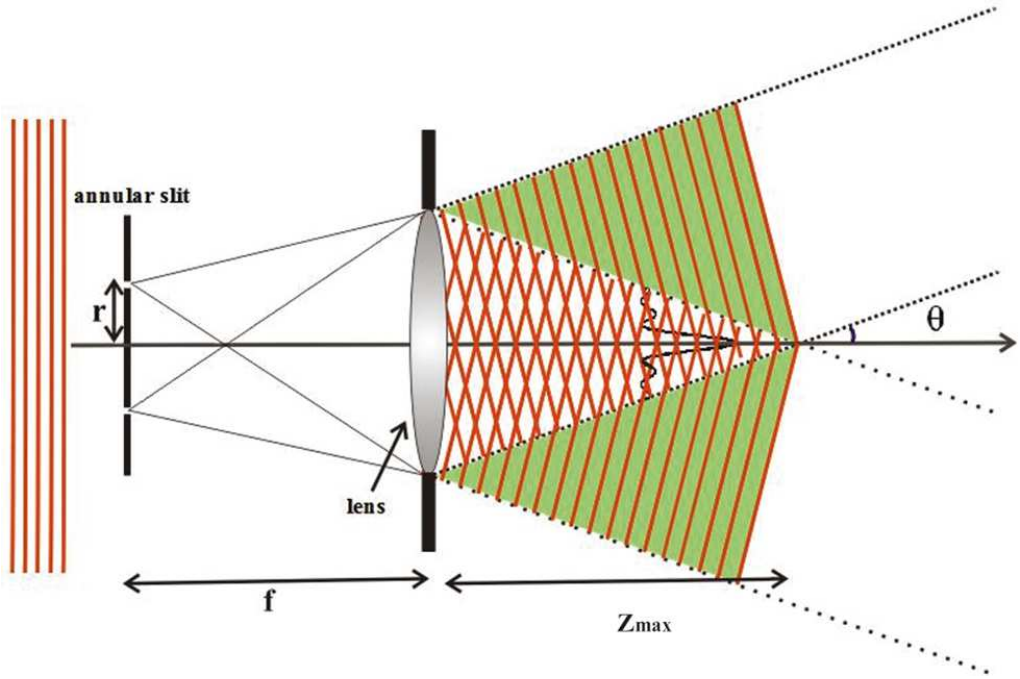

Figure 4.6: Pseudo-Bessel-beam generation using an annular slit diaphragm and a lens. Image taken from Anguiano-Morales et. al [11].

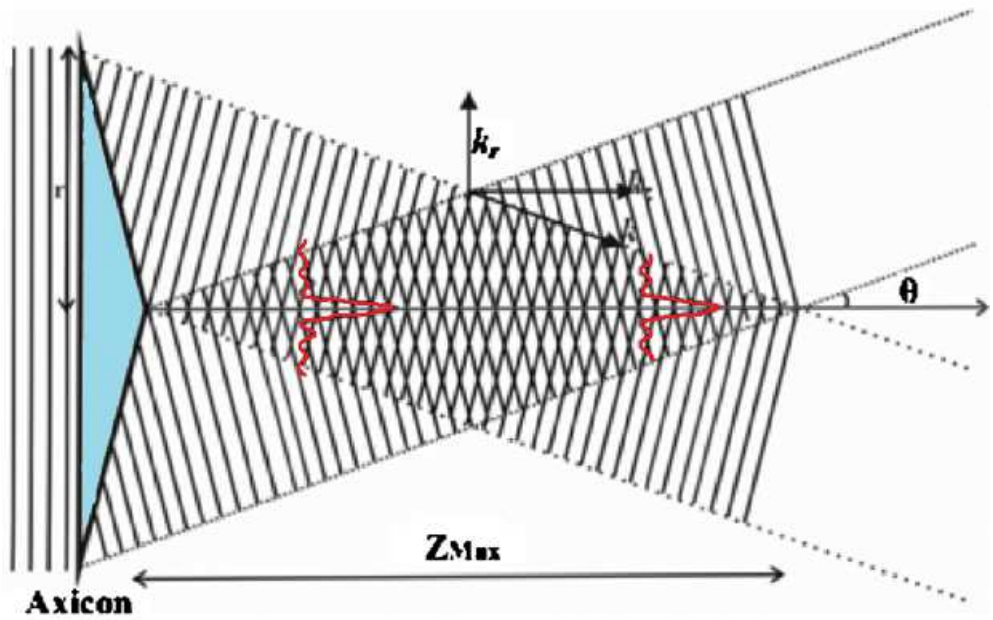

Figure 4.7: Pseudo-Bessel-beam generation using an axicon lens. Image taken from Anguiano-Morales et. al [11].

Chapter 5

Microwave Bessel-Beam Propagation

5.1 Numerical Simulation of Bessel-Beam

In order to investigate the propagation of a microwave Bessel-beam, one must first model the plane wave spectrum representation of the electromagnetic beam field in MATLAB. Creating the plane wave spectrum representation of the electromagnetic beam field of a Bessel-beam in cylindrical coordinates requires the implementation of several mathematical procedures related to the proper numerical implementation of the Quasi-fast Hankel transform (QFHT) and its inverse Quasi-fast Hankel transform (IQFHT) described in Appendix A. These include the application of a so-called guard band to minimize numerical aliasing errors.

The numerical implementation of a guard band is vital when creating the plane wave spectrum representation of an electromagnetic beam field. The purpose of the guard band is to pad zeros at the end of a signal out a certain distance in order

to minimize the effects of numerical aliasing. This distance measured is relative to the radius of the source aperture as well as the electromagnetic characteristics of the region into which the signal is propagated, taking into account the transverse spreading of the electromagnetic beam field as it propagates.

The QFHT algorithm is used here instead of the rectangular coordinate FFT in order to take advantage of the cylindrical symmetry of the Bessel-beam. The QFHT algorithm transforms a radially dependent field into an angular spectrum representation of plane waves. Each spectral component can then be propagated the distance z through multiplication by an exponential phase factor. The resulting spectrum is then transformed back into the radial space domain using the IQFHT. This propagation algorithm is described in Appendix B.

5.2 Transmission in Free Space

The primary effect that effects propagation through vacuum is diffraction and this is most conveniently described through the Fresnel number

$$N = \frac{a^2}{\lambda \Delta z}, \tag{5.1}$$

where a is the beam radius, λ is the wavelength, and Δz is the propagation distance. The simulations done in this research correspond to an aperture with a 25 meter radius and 1 degree structure angle corresponding to α in Eqs. (4.15 - 4.16). The following figures show the evolution of the radial electric field strength as the Bessel-beam propagates away from the initial plane through a vacuum.

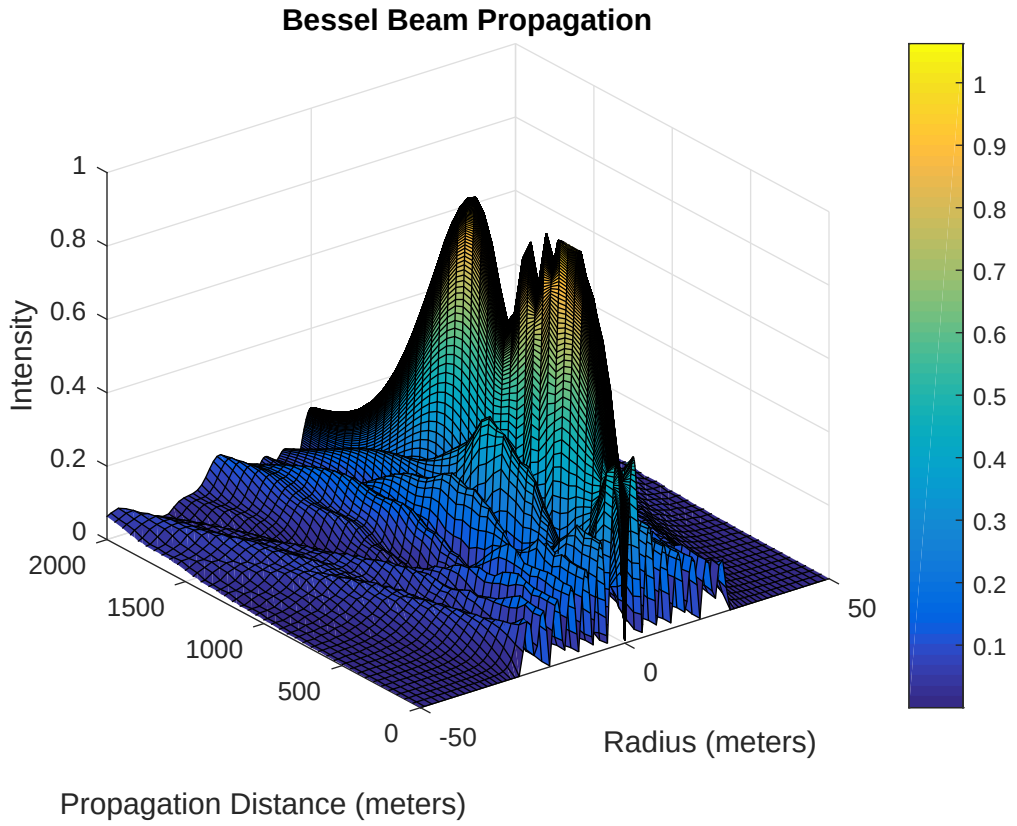

Figure 5.1: Surface plot depicts the relative intensity of the radial electric field (E_ρ) of a Bessel-beam as a function of the radius as the beam propagates over 2,000 meters from the source aperture in free-space.

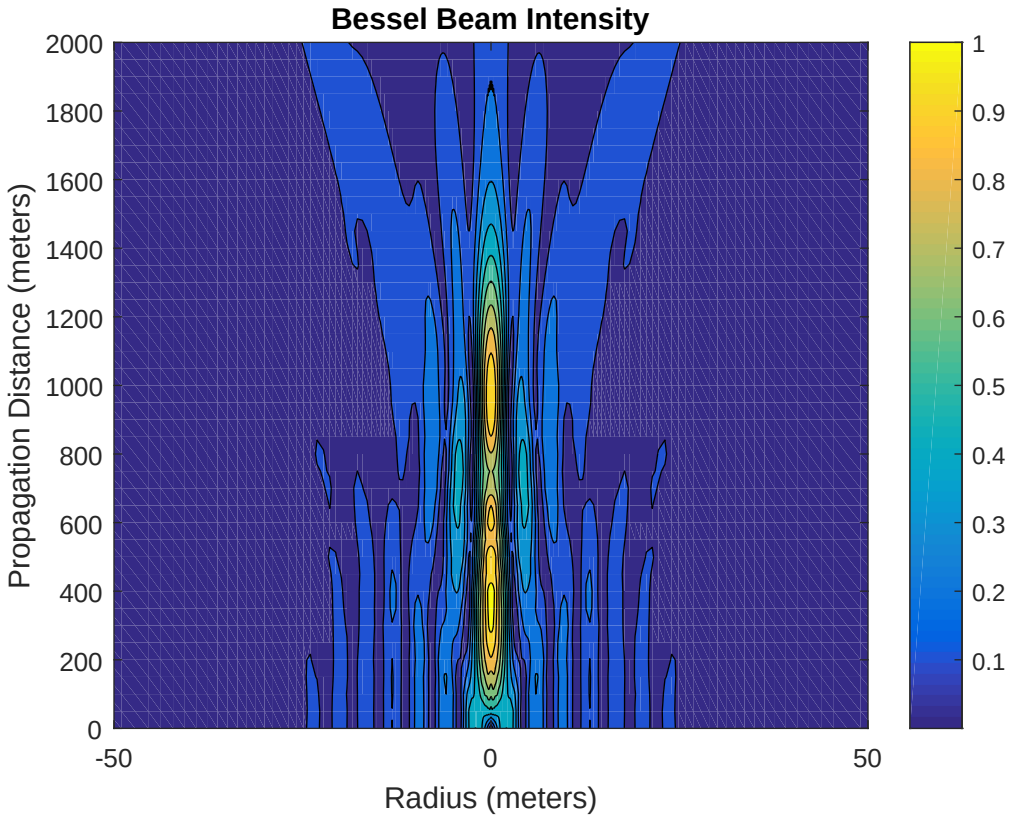

Figure 5.2: Contour plot depicting the intensity of the radial electric field (E_ρ) as a function of the radius as the beam is propagated 2,000 meters from the source aperture in free space. The largest contribution of constructive interference which creates this beam is shown at 500 and 1,000 meters.

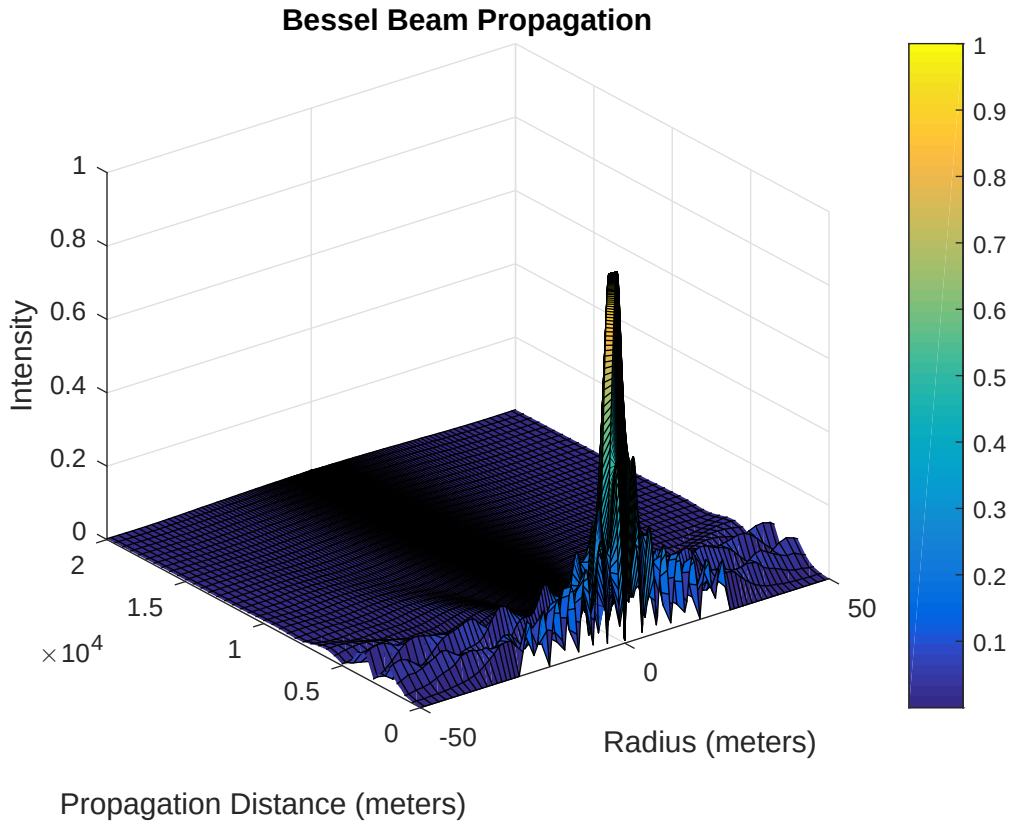

Figure 5.3: Surface plot depicting the relative intensity of the radial electric field (E_ρ) of a Bessel-beam as a function of the radius as the beam propagates over 20,000 meters from the source aperture in free-space.

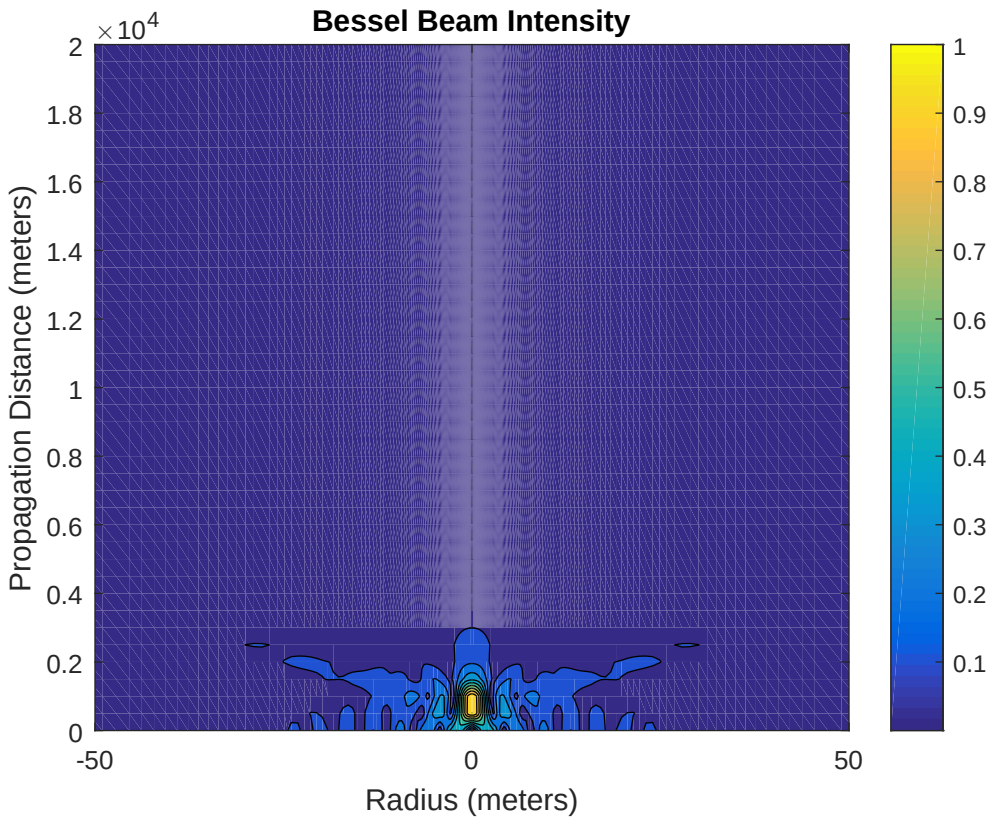

Figure 5.4: Contour depicting the amplitude of the radial electric field (E_ρ) as a function of the radius as the beam propagates over 20,000 meters from the source aperture in free-space.

The numerical results presented in Figs. 5.1-5.4 show that the distance the microwave Bessel-beam is propagated in free space has a very noticeable impact on the signal amplitude. The signal strength begins to rapidly deteriorate when it is propagated over 2,000 meters through a vacuum. The natural spreading of this beam over relatively long distances is the reason for this rapid decay. An aperture with a larger radius could overcome this problem theoretically, but in reality would cost much more.

5.3 Transmission through Spatially Inhomogeneous Media

The transmission of a microwave Bessel-beam through a spatially inhomogeneous medium is the central problem arising in atmospheric propagation. The dominant effect appearing in propagation in the vertical direction is the dependence of the dielectric permittivity $\epsilon(z)$ and electric conductivity $\sigma(z)$ on the altitude z. This dependence is described in Chapter 3. This variation has two effects on the transmitted electromagnetic field, particularly when it is discretized into a series of homogeneous slabs. The first is that only a fraction of the wave energy is transmitted at each interface between neighboring slabs, given by the normal incidence transmission coefficient τ_{ij} given in Eq. (3.8). The second part is given by the field contributions that are first reflected and then transmitted. This second part contains a countably infinite number of contributions with decreasing amplitude determined, in part, by the number of reflections that are experienced.

The zeroth-order approximation to the transmitted beam field is then given by

$$\tilde{\mathbf{E}}^{(0)} = \sum_{j=1}^{N} \tau_{j,j+1} \tilde{\mathbf{E}}_j \tag{5.2}$$

where $\tilde{\mathbf{E}}_j$ is the propagated wave field through the j^{th} slab due to the field $\tilde{\mathbf{E}}_{j-1}$. The first order correction to this zeroth-order wavefield is given by the field contribution which experiences one pair of reflections in the k^{th} slab, so that

$$\tilde{\mathbf{E}}^{(1)} = \left(\sum_{k=1}^{N} \Gamma_{k,k+1} \Gamma_{k-1,k} \delta \tilde{\mathbf{E}}_j \right) \left(\sum_{j=1}^{N} \tau_{j,j+1} \tilde{\mathbf{E}}_j \right) \tag{5.3}$$

where $\delta \tilde{\mathbf{E}}_j$ describes the field propagated one round trip through the k^{th} slab. Because $|\Gamma_{j,j+1}| \ll |\tau_{j,j+1}|$, this contribution is small compared to $\tilde{\mathbf{E}}^{(0)}$. Higher-order contributions $\tilde{\mathbf{E}}^{(2)}$, $\tilde{\mathbf{E}}^{(3)}$, ... corresponding to two, three, ... reflected round trips through a given slab will likewise be even smaller.

The numerical simulations that were performed in this research correspond to an aperture with a 25 meter radius and a 1 degree structure angle. Figs. 5.5-5.8 illustrate the zeroth-order radial electric field strength after the Bessel-beam was propagated through the Earth's atmosphere. These numerical results show that as the Bessel-beam is propagated a large distance its field intensity decays as the beam spreads radially. Notice that the electromagnetic characteristics of the ionized region of the Earth's atmosphere cause increased spreading of the Bessel-beam as compared to that in a vacuum. This is due to the conductivity in the ionized region.

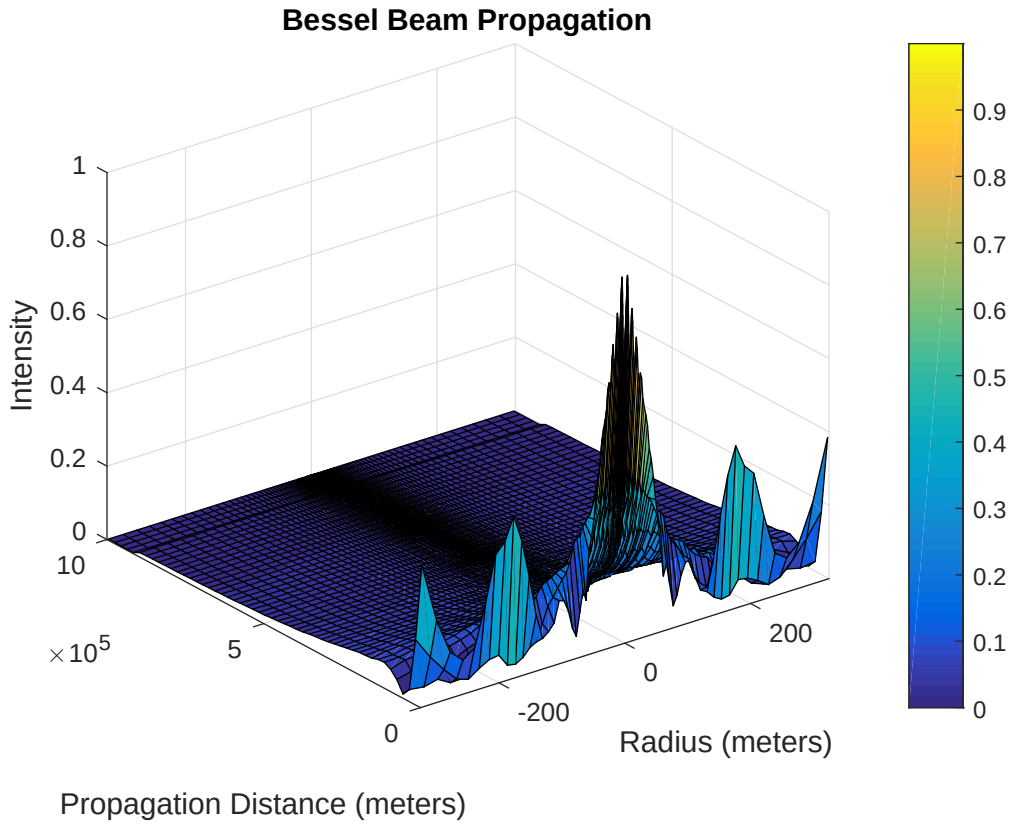

Figure 5.5: Surface plot depicting the intensity of the radial electric field (E_ρ) as a function of the radius corresponding to the distance the field is from the origin (1,000km above sea level) through the Earth's atmosphere to sea level.

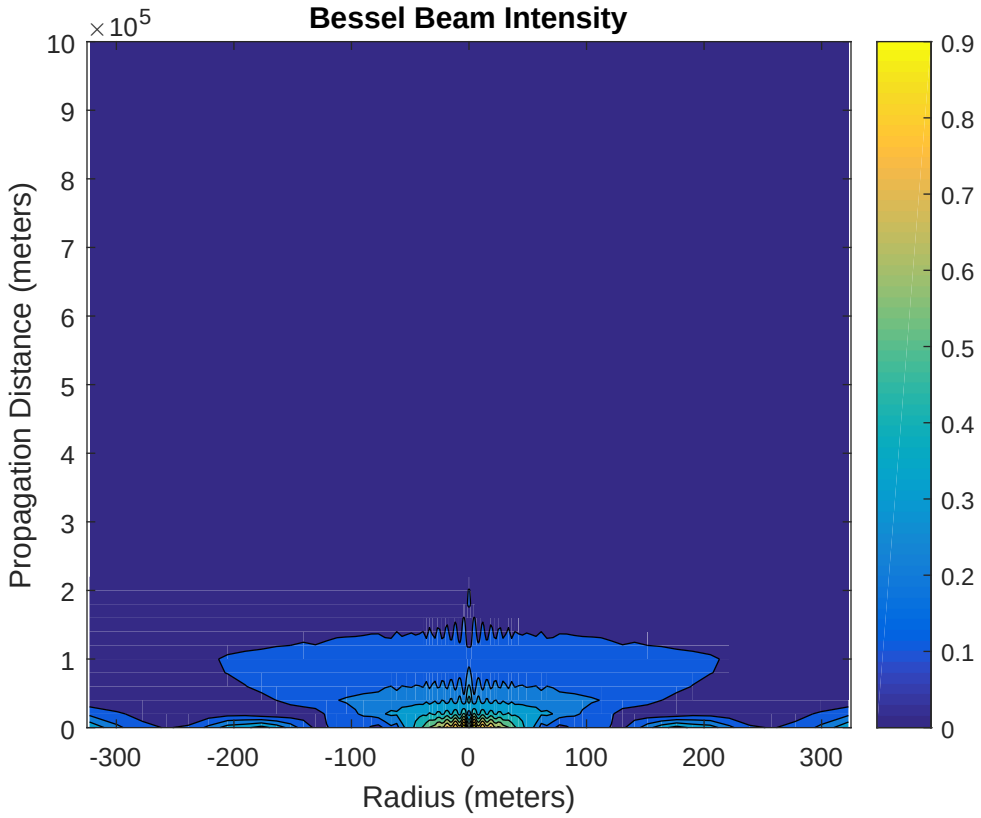

Figure 5.6: Contour plot depicting the intensity of the radial electric field (E_ρ) as a function of the radius corresponding to the distance the field is from the origin (1,000km above sea level) through the Earth's atmosphere to sea level.

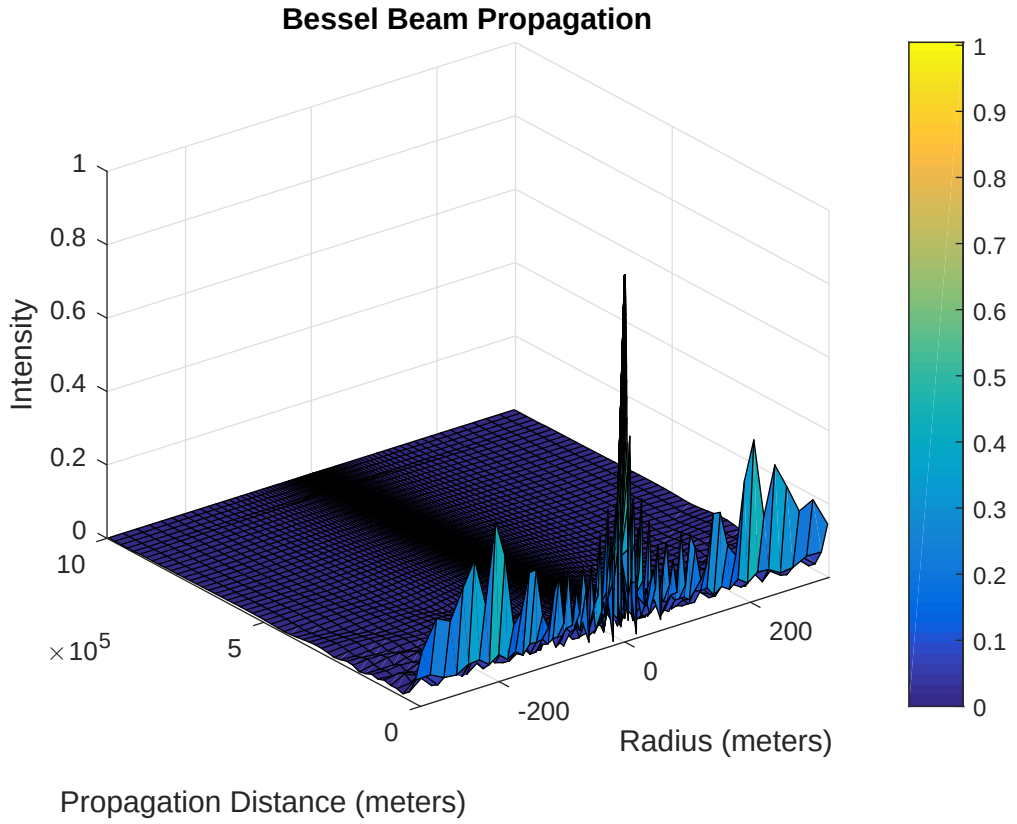

Figure 5.7: Surface plot depicting the intensity of the radial electric field (E_ρ) as a function of the radius corresponding to the distance the field is from the origin (1,000km above sea level) through the Earth's atmosphere to sea level. The aperture radius of the Bessel-beam was set at the guard band (325 meters).

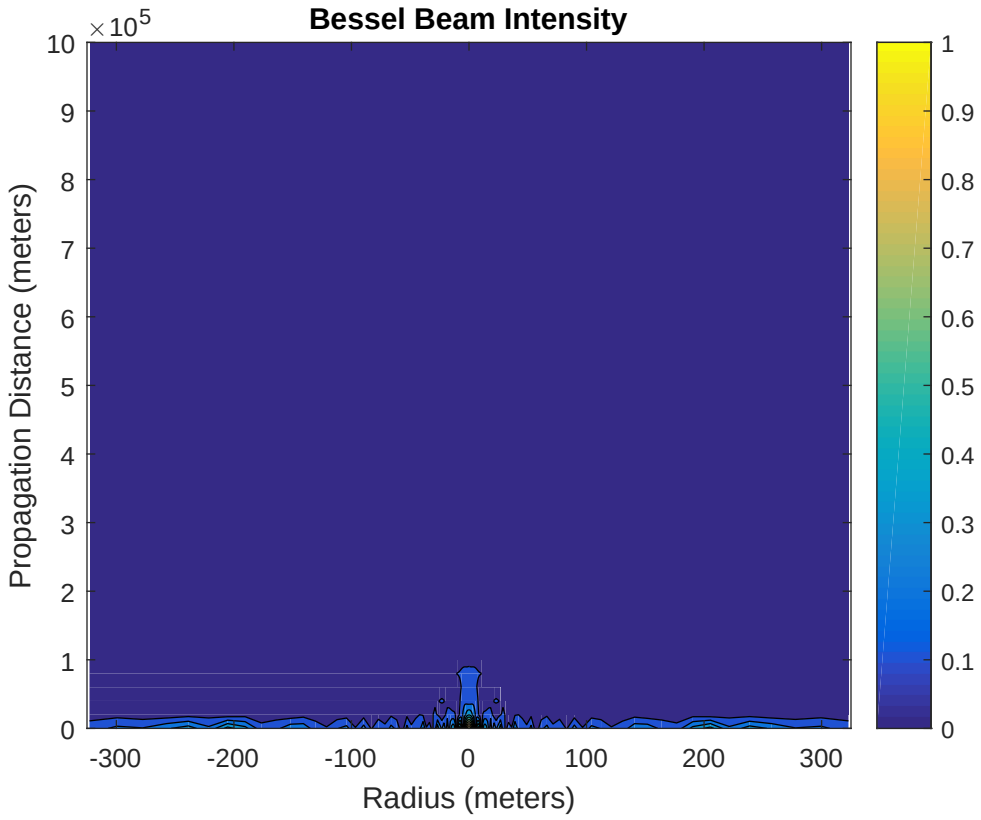

Figure 5.8: Contour plot depicting the intensity of the radial electric field (E_ρ) as a function of the radius corresponding to the distance the field is from the origin (1,000km above sea level) through the Earth's atmosphere to sea level. The aperture radius of the Bessel-beam was set at the guard band (325 meters).

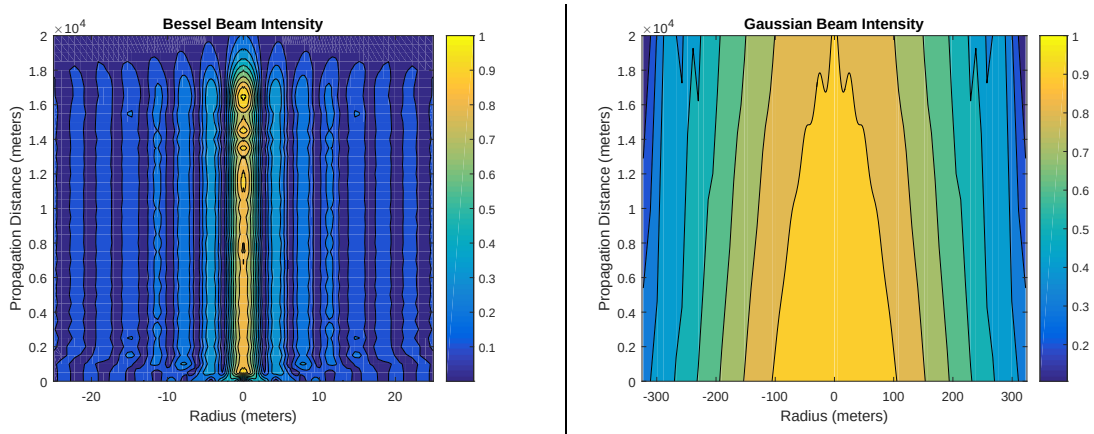

(a) Bessel-Beam (b) Gaussian Beam

Figure 5.9: Comparison of an Bessel-beam and Gaussian Beam truncated at the guard band (325 meters) after being propagated 20,000 meters in free space. Comparing the two plots it is clear that the Bessel beam intensity is much more concentrated in the center in comparison to the Gaussian Beam over this relatively small distance.

5.4 Beam Intensity Comparisons

The originating purpose of this research was to determine how well a microwave Bessel-beam can propagate with negligible diffractive spreading over some finite distance through a spatially inhomogeneous medium. This is done by comparing the Bessel-beam with an equivalent size Gaussian beam in each simulation. This equivalence was made by choosing an identical initial beam width for both beams. It is seen in Figs. 5.9-5.12 that this Gaussian beam has seemingly better propagation characteristics than does the Bessel-beam over long distances. Although neither of the beams maintain their signal intensity throughout the full propagation distance, the Gaussian beam does appear to "maintain" its intensity over a longer propagation distance.

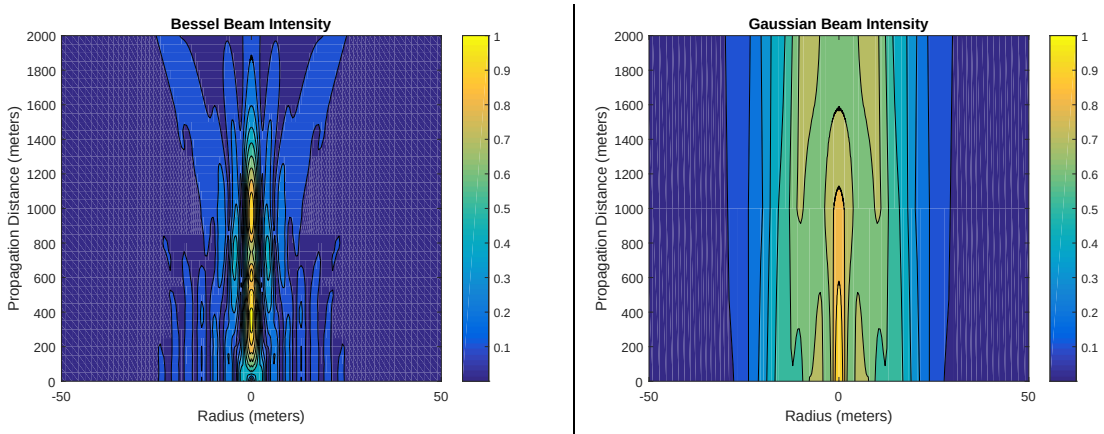

(a) Bessel-Beam (b) Gaussian Beam

Figure 5.10: Comparison of a Bessel-beam and its equivalent Gaussian Beam after being propagated 2,000 meters in free space. Comparison of the two plots show that the Bessel-beam intensity is much more concentrated in the center in comparison to the Gaussian Beam over this relatively small distance.

5.5 Power Transmission Comparisons

The power within a certain radial distance from the beam axis at a given propagation distance z can be determined by calculating the area under the transverse field intensity at z using a simple trapezoidal approximation. With the purpose of this research being to investigate power transmission capabilities of a microwave Bessel-beam this is a vital result.

The total power was calculated for a Bessel-beam and a Gaussian beam within a 1, 5, and 25 meter radius region. The results were plotted for each beam on the respective line plots. The power was calculated for 2,000 and 20,000 meters propagation distances for each beam. These arbitrary distances were chosen for consistency and because they portray vital power transmission results for each beam.

It is shown in the accompanying figures that over longer distances and within

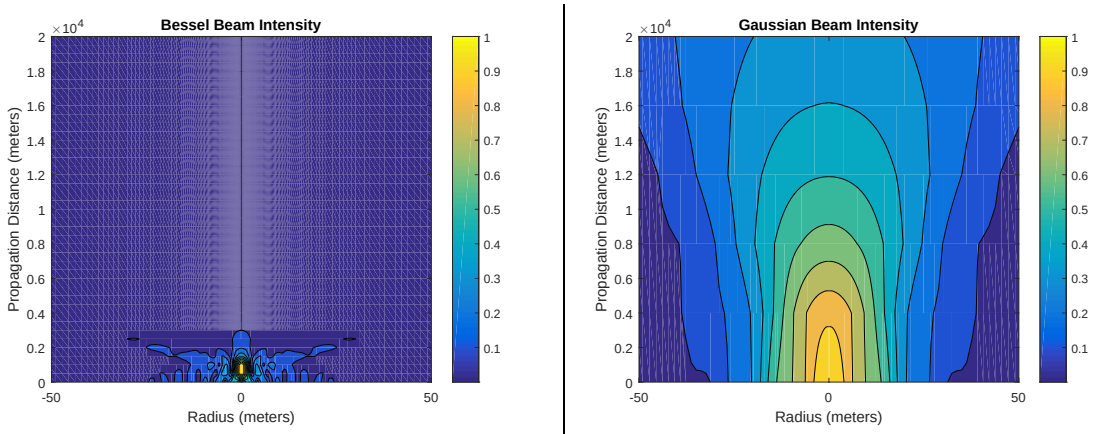

(a) Bessel-Beam (b) Gaussian Beam

Figure 5.11: Comparison of Bessel-beam and Gaussian Beam after being propagated 20,000 meters in free space. Comparison of the two plots show that the Gaussian beam intensity does not decay nearly as fast as the Bessel-beam does in regards to distance propagated.

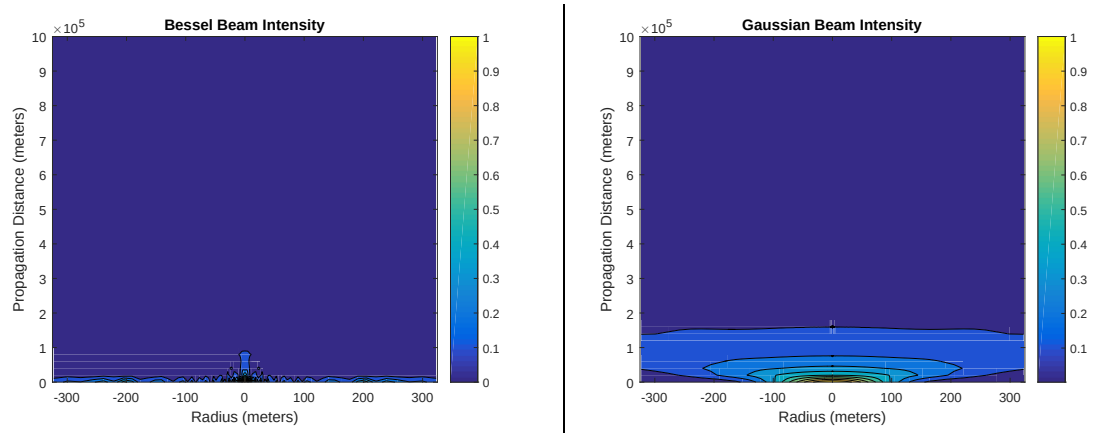

(a) Bessel-Beam (b) Gaussian Beam

Figure 5.12: Comparison of a Bessel-beam and Gaussian Beam after being propagated from the origin (1,000km above sea level) through the Earth's atmosphere to sea level. In this simulation both beams were truncated at the guard band (325 meters). As the beams transitions from the ionized region to the non-ionized region they lose almost all of there beam intensity.

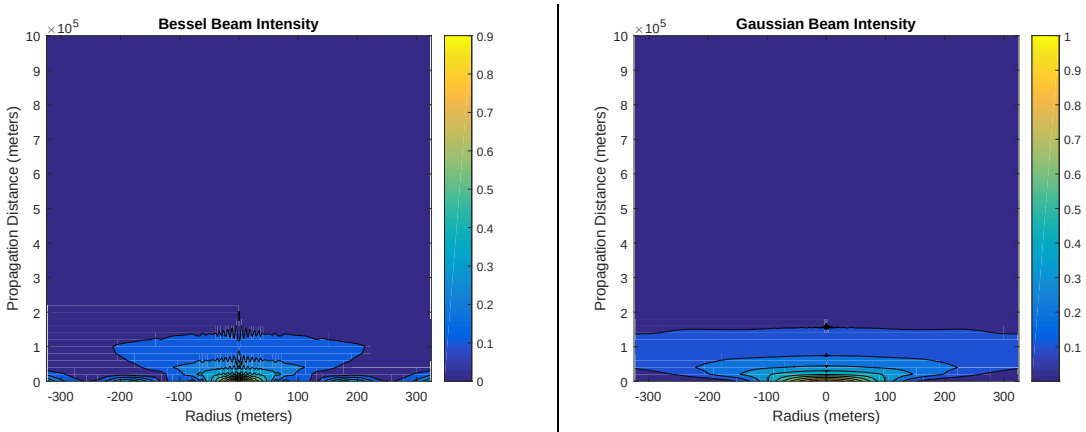

(a) Bessel-Beam (b) Gaussian Beam

Figure 5.13: Comparison of Bessel-beam and Gaussian Beam after being propagated from the origin (1,000km above sea level) through the Earth's atmosphere to sea level. As the Gaussian beam transitions from the ionized region to the non-ionized region it loses almost all of its beam intensity.

larger radial regions, the Gaussian beam delivers more power than does a truncated Bessel-beam. The only instance where a Bessel-beam performs better then a Gaussian beam is within a 1 meter radial region over propagation distances within the Bessel-beams non-diffractive region.

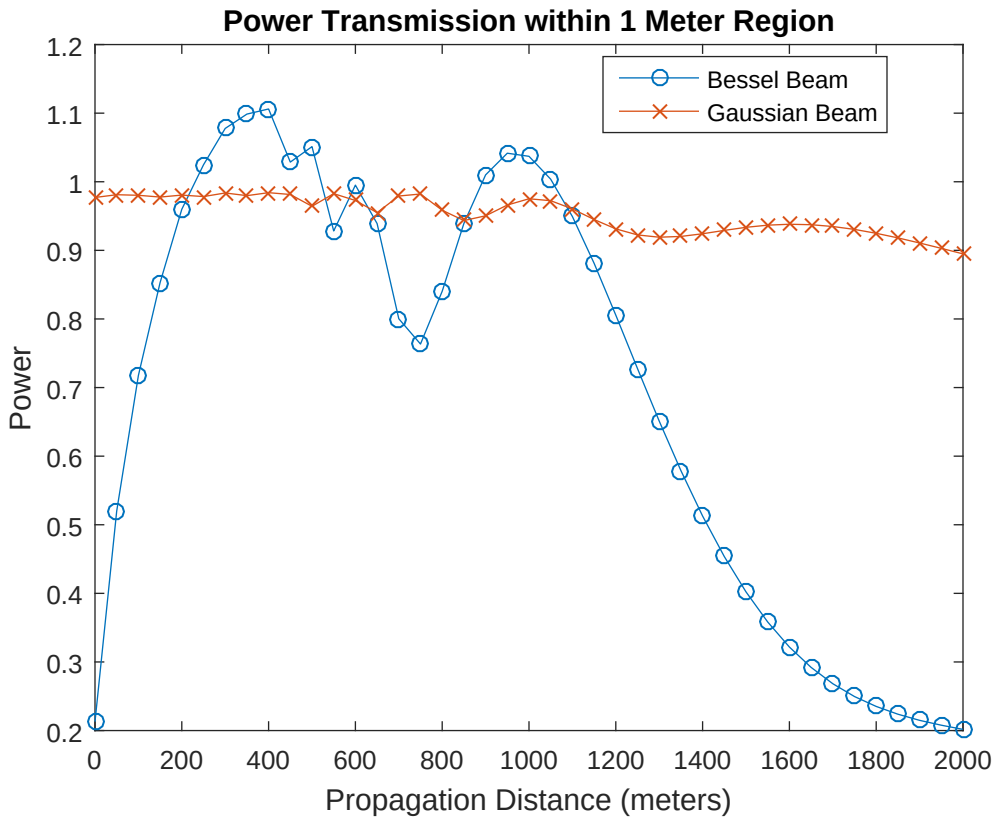

Figure 5.14: Comparison of a Bessel-beam and Gaussian beam power transmission quantities within a 1 meter radius area over a propagation distance of 2,000 meters.

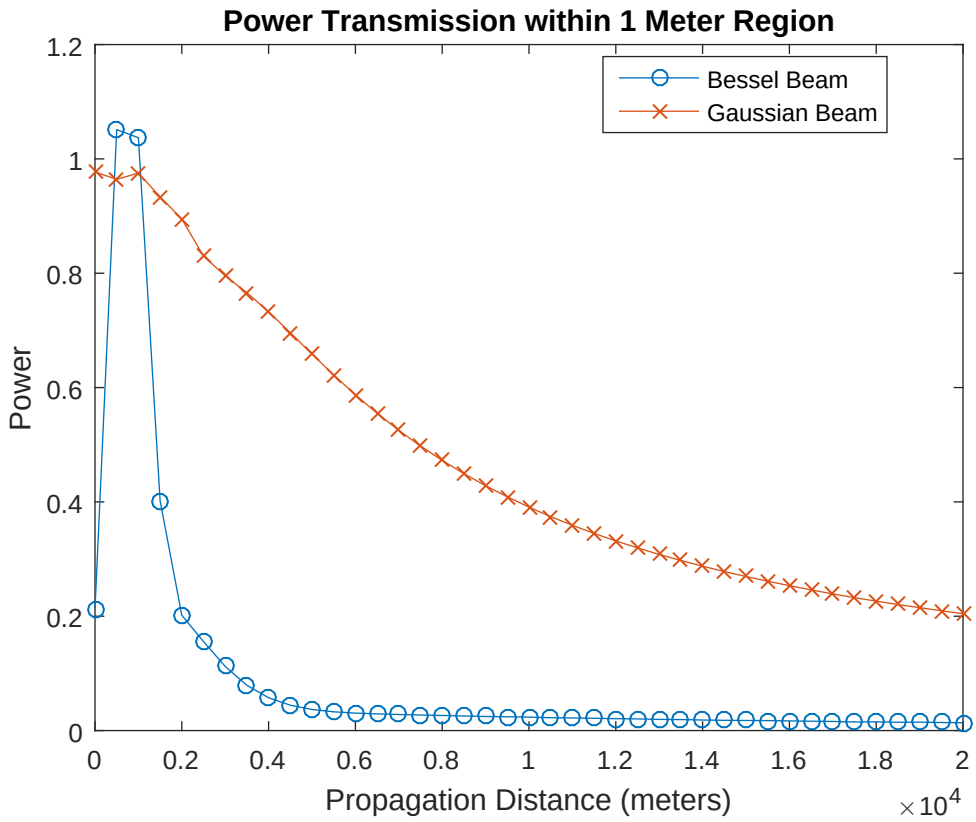

Figure 5.15: Comparison of a Bessel-beam and Gaussian beam power transmission quantities within a 1 meter radius area over a propagation distance of 20,000 meters.

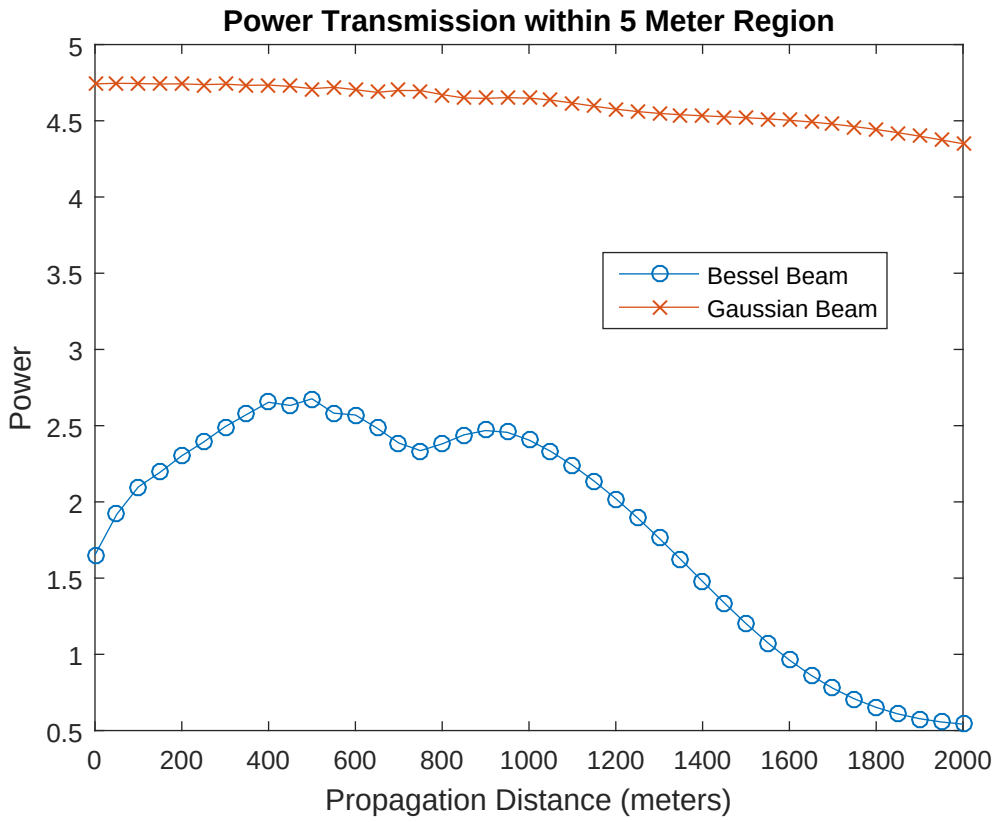

Figure 5.16: Comparison of a Bessel-beam and Gaussian beam power transmission quantities within a 5 meter radius area over a propagation distance of 2,000 meters.

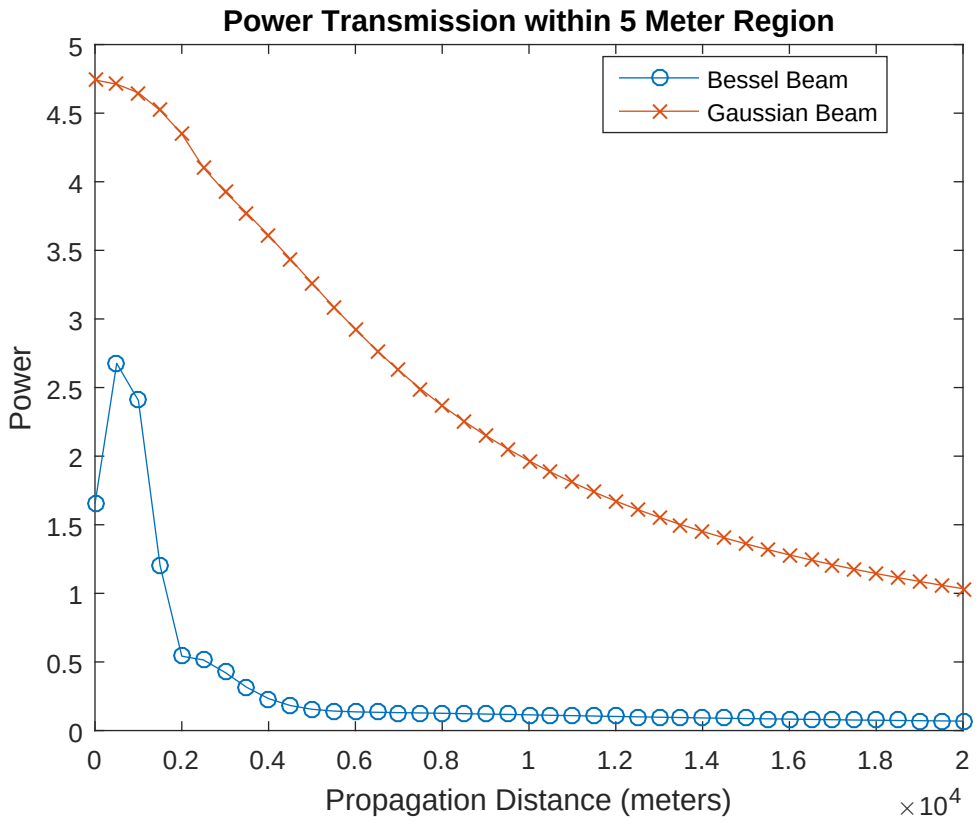

Figure 5.17: Comparison of a Bessel-beam and Gaussian beam power transmission quantities within a 5 meter radius area over a propagation distance of 20,000 meters.

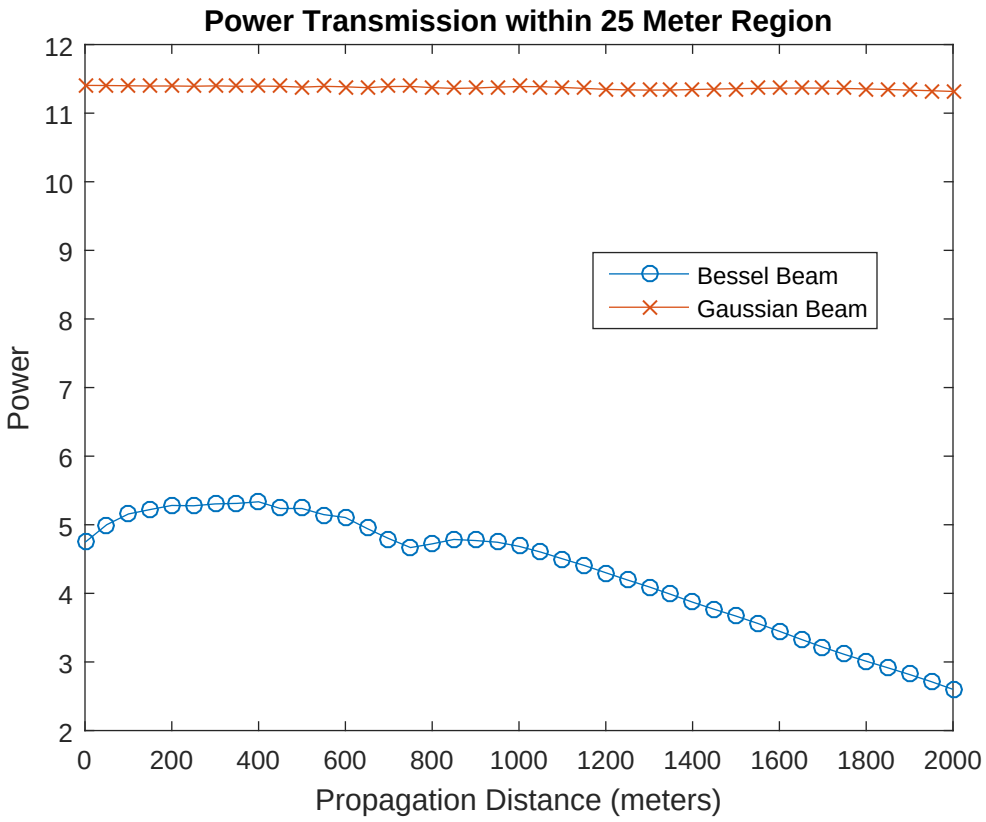

Figure 5.18: Comparison of a Bessel-beam and Gaussian beam power transmission quantities within a 25 meter radius area over a propagation distance of 2,000 meters.

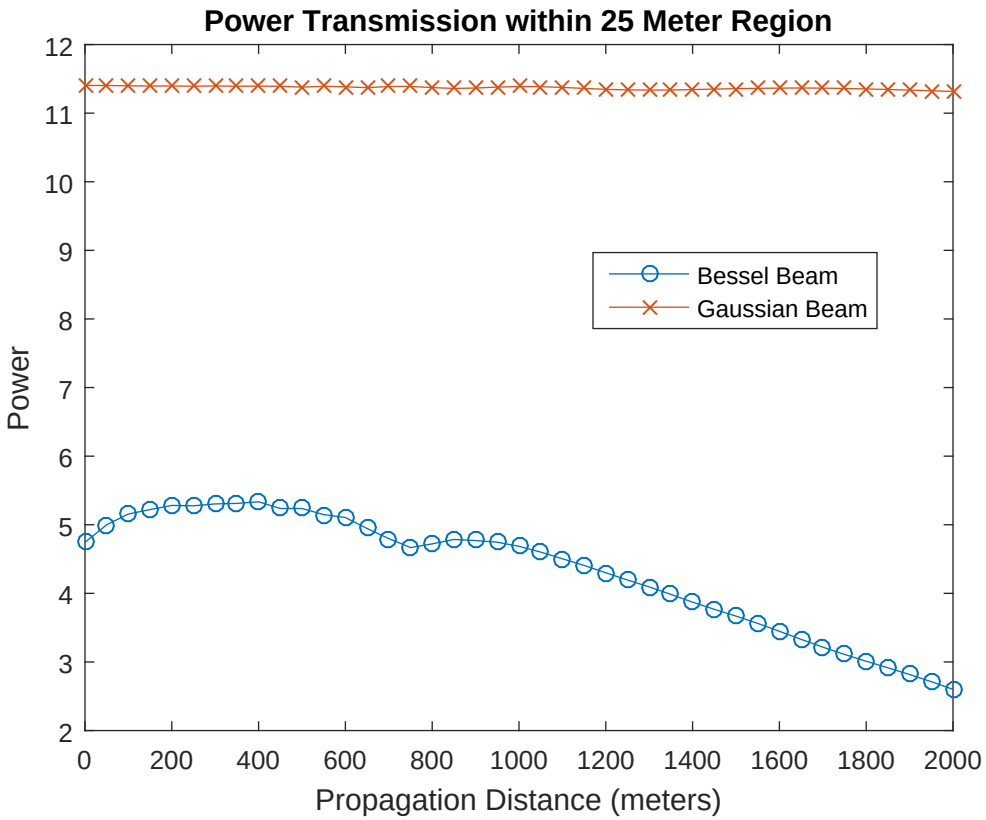

Figure 5.19: Comparison of a Bessel-beam and Gaussian beam power transmission quantities within a 25 meter radius area over a propagation distance of 20,000 meters.

Chapter 6

Conclusions

The numerical results presented in this research lead to the following conclusions:

1. Propagation Properties through Free Space

   (a) The Bessel-beam with an aperture radius equal to the guard band (325 meters) has a beam intensity more concentrated at the radial origin than the equivalent size Gaussian beam over the same propagation distance. The Gaussian beam also spreads faster than the Bessel-beam over the same propagation distance.

   (b) The Bessel-beam truncated at 25 meters has a beam intensity more concentrated at the radial origin than the Gaussian beam over a 2,000 meter propagation distance. However, in this same instance the Bessel-beam intensity rapidly decays to zero past approximately 2,000 meters. In comparison, the Gaussian beam maintains its beam intensity over this same distance.

(c) In conclusion, a Bessel-beam with a 25 meter aperture would only be more effective then a like Gaussian beam within its non-diffractive region in free space.

2. Propagation Properties through a Spatially Inhomogeneous Medium

   (a) The Bessel-beam truncated at the guard band (325 meters) has a beam intensity that is more concentrated at the radial origin than the Gaussian beam as they are propagated through the Earth's atmosphere. The beam intensity's decay within the ionized region.

   (b) In conclusion, propagation through the ionized region of the Earth's atmosphere only causes both beams to decay more rapidly. Wireless power transmission using either of these two beams through the Earth's atmosphere would not be efficient.

6.1 Future Research

Two things need to be done:

1. Small scale experiments.

2. More detailed calculations of atmospheric propagation.

References

[1] J. Durnin, "Exact solutions for nondiffracting beams. i. the scalar theory," *J. Opt. Soc. Am.*, 1987.

[2] N. Tesla, "Experimants with alternate currents of high potential and high frequency," in *lecture before the Institution of Electrical Engineers*.

[3] D. J. Griffiths, *Introduction to Electrodynamics Fourth Edition*. Pearson, 2013.

[4] W. C. Brown, "Experimental airborne microwave supported platform," tech. rep., Air Force Systems Command, 1965.

[5] R. M. Dickinson, "Evaluation of microwave high-power reception-conversion array for wireless power transmission," tech. rep., National Aeronautics and Space Administration, 1975.

[6] K. E. Oughstun, *Electromagnetic and Optical Pulse Propagation 1 Spectral Representations in Temporally Dispersive Media*. Springer, 2006.

[7] S. J. Robbins, "Elemental composistion of mars' atmosphere," tech. rep., Case Western Reserve University Depeartment of Astronomy, 2006.

[8] K. A. Dao, V. P. Tran, and C. D. Nguyen, "The wireless transmission environment from geo to the earth and numerical estimation of relative permittivity vs the altitude in the neutral and ionized layers of the earth atmosphere," in *Proceeding of The 2014 International Conference on Advanced Technologies for Communications (ATC-14)*.

[9] R. A. Chipman, *Schaum's Outline of Theory and Problems of Transmission Lines*. McGraw-Hill, 1968.

[10] K. T. McDonald, "Bessel beams," tech. rep., Joseph Henry Laboratories, Priceton University, 2000.

[11] M. Anguiano-Morales, "Generation of a spiral wave by modified annular slit," *Opt. Eng. 50(7)*, 2011.

[12] E. W. Weisstein, "Hankel transform," tech. rep., From MathWorl–A Wolfram Web Resource, 2016.

[13] A. E. Seigman, "Quasi fast hankel transform," *Opt. Lett. 1, 13*, 1977.

Appendix A

Hankel Transform

The Hankel transform is derived here from the 2D-Fourier transform in (x, y) coordinates through a coordinate change to polar coordinates (r, θ). The Hankel transform of order zero is an integral transform equivalent to a 2D-Fourier transform with a radially symmetric integral kernel. This is defined as [12]

$$g(u, v) = \int_{-\infty}^{\infty} \int_{-\infty}^{\infty} f(r) e^{-2\pi i(ux+vy)} dxdy. \tag{A.1}$$

Let

$$x + iy = re^{i\theta}, \tag{A.2}$$

and

$$u + iv = qe^{i\phi}, \tag{A.3}$$

so that $x = r\cos\theta$, $y = r\sin\theta$, where

$$r = \sqrt{x^2 + y^2}, \tag{A.4}$$

and $u = q\cos\phi$, $v = q\sin\phi$, where

$$q = \sqrt{u^2 + v^2}. \tag{A.5}$$

Then

$$g(q) = \int_0^\infty \int_0^{2\pi} f(r) e^{-2\pi i r q \cos\theta} r dr d\theta \tag{A.6}$$

so that

$$g(q) = 2\pi \int_0^\infty f(r) J_0(2\pi q r) r dr \tag{A.7}$$

where $J_0(z)$ is the zeroth order Bessel function of the first kind.

A.1 Quasi-Fast Hankel Transform

Testing the Quasi-fast Hankel transform (QFHT) was necessary in order to prove it yields correct results when applied to the Bessel-beam. This was done by comparing the results of two different mathematical procedures performed on specific functions. One mathematical procedure being the integration of the zeroth order Bessel function and the other performing the QFHT on the unit step function. If the QFHT is working properly these will yield the same results, possibly with some correction constant.

The Hankel transform of the circle function $f(r) = 1$ for $r \leq 1$ and $f(r) = 0$ for $r > 0$ is given by

$$2\pi \int_0^1 J_0(2\pi k r) r dr = 2\pi \frac{J_1(2\pi k)}{2\pi k} \tag{A.8}$$

where the limits 0 and 1 in the integral are determined by the Hankel transform itself (the lower bound) and by the circle function (both lower and upper bounds). The

code used to perform the QFHT is shown below:

```
% Quasi-Fast Hankel Transform
K = w/c0;                          % maximum spatial frequency
R = 25;     % maximum radius
n=0;
M=7;
m=5;
a=K*R/2/pi;
N=pow2(ceil(1 + log2(a*m*log(a*M))));
a=1/a/m;
ro=R*exp(-a*N/2);
ko=K*exp(-a*N/2);
I=exp(a*(0:N-1));
k=ko*I(1:N/2);                          % samplings
r=ro*I(1:N/2);
I=ifft(a*ko*ro*I.*besselj(n,ko*ro*I)); % kernel

h = [ones(1,4900), zeros(1,3292)];     % unit step function

H=fft(fft(h.*r,N).*I);                 % transform
H=real(H);
H=2*pi*H(1:N/2)./k;
```

A radial plot of the unit circle function is shown in Fig. A.1. Using the resulting spatial frequency (k) values computed in the algorithm the QFHT calculation of the spectrum (H) of this unit circle function can then be compared to the analytic integration result given in Eq. A.7 in order to demonstrate its degree of accuracy. The comparison is given in Fig. A.2. The zeroes of the Bessinc function in Eq. (A.8) occur at the zeroes of the $J_1(\rho)$ Bessel function excluding the zero at the origin. A comparison of the zeroes for the QFHT calculation with these analytic values along with the accompanying percent differences are given in table A.1, showing that the error is below 0.5%.

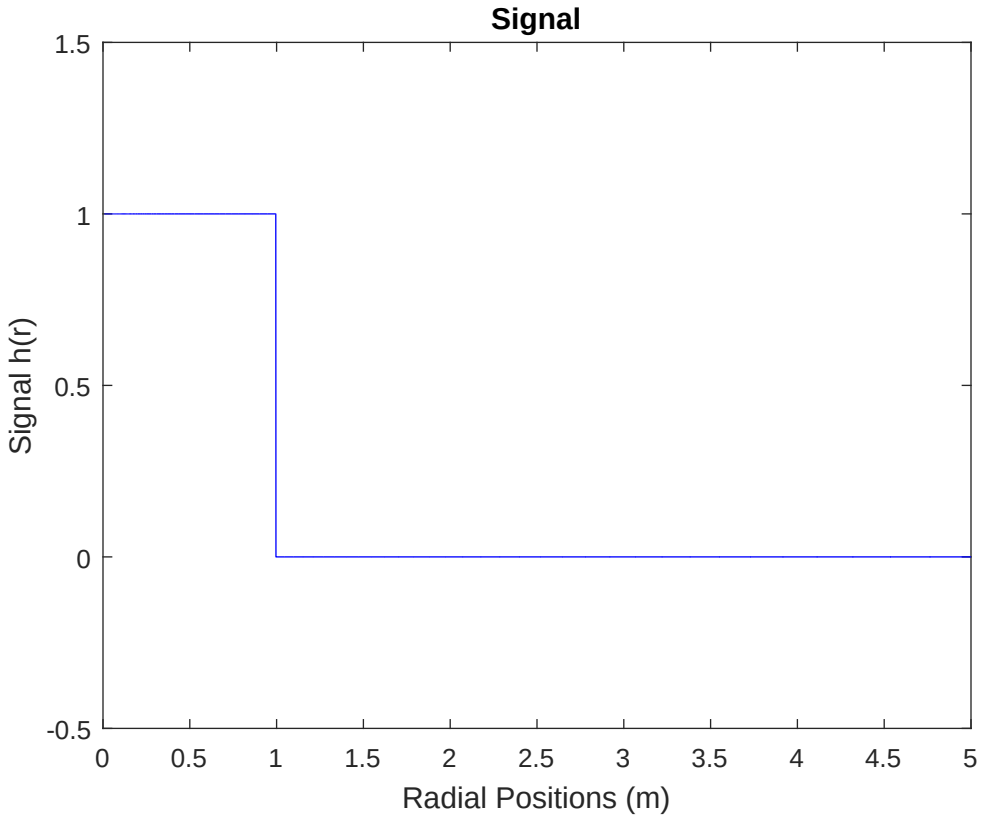

Figure A.1: Radial plot of the unit step function. The signal has a value of 1 from the origin out to a radius of 1 meter and is zero for all larger values of r. The computational domain, which must be finite, extends out to 25 meters so that there is a so-called guard band ratio of 25/1 [13].

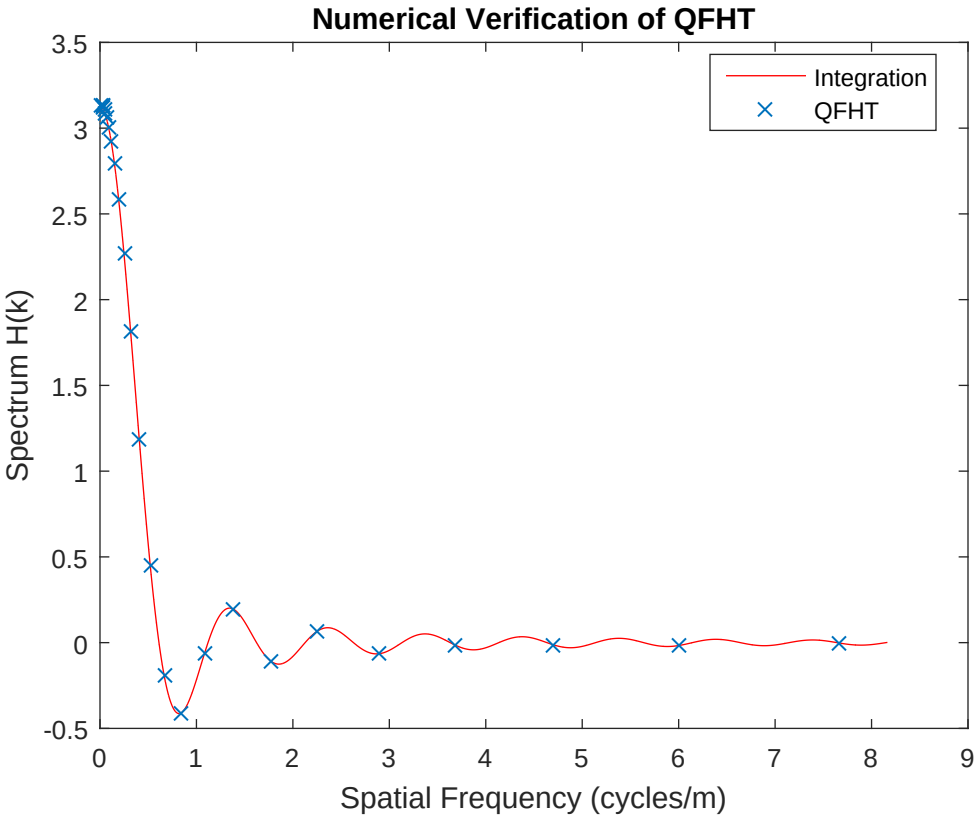

Figure A.2: Plot depicting the results and comparison of the QFHT to direct integration. It is seen that the integration results overlap the QFHT results. A comparison of the QFHT zeros the the integration zeros along with the percent difference are given in table A.1. The nonlinear radial spacing used in the QFHT is equivalent in the figure

Table A.1: Zeroes Comparison

n	$J_1(x_n) = 0$ x_n	Integration $x_n/2\pi$	QFHT	Percent Difference
1	3.832	0.609835	0.612349	0.411388%
2	7.016	1.116565	1.121391	0.431275%
3	10.173	1.619158	1.625748	0.406191%
4	13.323	2.120531	2.129798	0.436083%
5	16.470	2.621382	2.631958	0.402637%
6	19.612	3.121961	3.135691	0.438819%
7	22.760	3.62238	3.636885	0.399629%
8	25.903	4.122697	4.140943	0.44158%
9	29.047	4.622971	4.641339	0.396529%
10	32.190	5.123147	5.145943	0.443984%
11	35.332	5.623311	5.645556	0.394805%
12	38.475	6.123449	6.150828	0.446118%
13	41.617	6.623566	6.649634	0.392786%
14	44.759	7.123667	7.155656	0.448054%
15	47.901	7.623754	7.653616	0.390922%

Appendix B

Microwave Bessel-Beam Propagation

In order to create the plane wave spectrum representation of a microwave Bessel-beam, several specific steps need to be taken. Because the radial component of the electric field, given by

$$E_\rho = \cos\alpha J_1(k\rho\sin\alpha)e^{i(kz\cos\alpha-\omega t)} \tag{B.1}$$

is the focus of this research, numerical values for the initial beam parameters must first be defined. The angle (α) and radius (r) of the aperture were chosen to be 1 degree and 25 meters, respectively. The frequency of the beam was chosen to be 2.45 GHz. The wave number can then be calculated from these values. The code implementing these mathematical steps is given below:

```
% Initial Beam Parameters
c0 = 299792458;         % speed of light in a vacuum
f = 2.45*10^9;          % microwave frequency
```

```
w = 2*pi*f;             % angular frequency
alpha = 0.0174533;      % angle
R = 25;                 % maximum radius
kk_z = (w*cos(alpha))/c0;         % longitudinal wave number
kk = kk_z/cos(alpha);             % wave number
K = w/c0;                         % maximum spatial frequency
kk_rho = kk*sin(alpha);           % radial wave number
lambda0 = c0/f;
```

Prior to implementing a QFHT on the Bessel-beam equation a guard band ratio must be determined. A numerical guard band accounts for the region outside of the initial region of propagation into which the numerically determined field may spread upon propagation due to diffraction. This calculation region is initially padded with zeroes prior to the implementation of a QFHT. In order to calculate how large this guard band must be, several characteristics regarding the propagation geometry must be known. These include the maximum index of refraction the beam is propagating through, the distance the beam is propagating, the initial radius of the beam, the allowable numerical spill-over error, and the frequency. The code implementing these mathematical steps is given below:

```
Nmax = sqrt((23.4377)^2 + (23.4163)^2);
lambda = (c0)/(f*Nmax);
Nc = (R^2)/(lambda*20000);
Ep1 = 0.001;
Gmin = 1+(2*pi^2*Nc*Ep1)^(-1) * (1+sqrt(1+pi*Ep1));
R = R*Gmin;
```

Here Gmin is the guard band ratio and R is the total region being investigated after propagation. The QFHT is then applied to the initial Bessel-beam in order to compute the corresponding initial spectrum. The code implementing these mathematical steps is given below:

```
% Define electric field equation
h=@(r)( cos(alpha).*besselj(1,r*kk*sin(alpha)) );

n=0;
M=7;
m=5;

a=K*R/2/pi;
N=pow2(ceil(1 + log2(a*m*log(a*M))));
a=1/a/m;
ro=R*exp(-a*N/2);
ko=K*exp(-a*N/2);
I=exp(a*(0:N-1));
k=ko*I(1:N/2);                          % samplings
r=ro*I(1:N/2);
I=ifft(a*ko*ro*I.*besselj(n,ko*ro*I)); % kernel
h=feval(h,r);
h = h(1:end-34000);
h = [h, zeros(1,34000)];                % zero padding guard band
H=fft(fft(h.*r,N).*I);                  % transform
H=real(H);
H=2*pi*H(1:N/2)./k;

k = k./(2*pi);
```

Once the initial spectrum has been computed, the beam spectrum is then propagated a specific distance Δz=dis through the medium with index of refraction (n_c) through multiplication by the exponential factor $e^{(i\beta\Delta z)}$. An example of this calculation for a distance of 1,000 meters is provided in the code below:

```
lambda = lambda0/n_c(1);
beta = (2*pi/real(lambda))*(1-real(lambda)^2.*k.^2).^(1/2);
alpha = 1i*((2*pi/imag(lambda))*(1-imag(lambda)^2.*k.^2).^(1/2));
Beta = beta + alpha;
dis = 1000;
H = H.*exp(1i*Beta*dis);
```

This propagation process then results in an altered spectrum. The IQFHT is then applied to this propagated beam spectrum, resulting in the propagated field at the specified distance.